that modify proteins and nucleic acids (5). Therefore, as reported, lipid peroxidation in the brains of AD patients not only harms cells but increases levels of such peroxidation products as thiobarbituric acid-reactive substances (10), acrolein-deoxyguanosine adducts (9), and cytotoxic compounds such as acrolein (12) and 4-hydroxynonenal (HNE) (17).

Lipid peroxidation propagates itself by autoxidation initiated by free radicals and produces considerable amounts of secondary products before the process terminates (21). These well-known secondary products include reactive aldehydes, such as acrolein, malondialdehyde, HNE, and 4-hydroxyhexenal (5). HNE is product that results from the lipid peroxidation of n-6 PUFAs, *e.g.*, linoleic acid and arachidonic acid (5). Because the brain is rich in arachidonic acid (29), lipid peroxidation tends to produce HNE at that site. These substances then react with proteins, nucleic acids and small molecules such as glutathione in cells and eventually impair normal biological functions of the essential components (5). Indeed, HNE is cytotoxic for cultured neuronal cells (2, 5, 8, 15). Therefore, HNE might induce neuronal cell death and neurodegeneration in patients with AD.

Measuring the exact quantity of HNE *in vivo* is difficult, since they are rapidly consumed when their chemically active aldehyde reacts with such cellular components as glutathione, proteins and nucleic acids (5). HNE reacts with lysine, histidine and cysteine residues in proteins to form Michael adducts and also Schiff base products (lysine ε-NH_2). When HNE reacts with proteins, HNE-histidine Michael adduct is a major product that develops in the cyclic hemiacetal form (3, 27). Because the cyclic hemiacetal form of HNE is relatively stable (5), the detection of HNE Michael adduct is considered a reliable index of lipid peroxidation. This property enabled us to measure HNE-histidine Michael adduct using the specific antibody to cyclic hemiacetal type of HNE-histidine Michael adduct.

To clarify the influence of lipid peroxidation on the pathogenesis of AD, we directly assessed the cyclic hemiacetal type of HNE-histidine Michael adduct in brain specimens from AD subjects and age-matched controls. As a result, the HNE adduct was detected in the hippocampi of both groups, especially the CA2, CA3 and CA4 sectors. The important difference was significantly higher levels of the HNE adduct in the brains of patients with AD. This is the first report of specific antibody usage for direct detection of HNE-histidine Michael adduct in the cyclic hemiacetal form within hippocampi from humans with AD.

MATERIALS AND METHODS

Human subjects. All clinical data from patients and information at autopsies from four patients with AD (two women and two men) and four (one women and three men) normal (no AD), age-matched subjects who died during the last several decades were retrieved from the autopsy database of the Department of Tokyo Metropolitan Geriatric Hospital, Tokyo, Japan. Brain specimens were registered in the Brain Bank for Aging Research (BBAR) organized by Tokyo Metropolitan Geriatric Hospital and Tokyo Metropolitan Institute of Gerontology (TMIG). Brain specimens used in this study were from patients clinically diagnosed as having AD-positive and control subjects without any sign of AD. All AD patients met accepted criteria for the neuropathologic diagnosis of AD based on the National Institute of Aging (NIA)-Reagan Institute Criteria for the Neuropathological Diagnosis of AD (1997) (1), combining abundant neuritic plaques in the neocortex (definite AD with consortium to establish a registry for AD criteria) and a profusion of NFTs in the limbic and neocortical areas (Braak and Braak staging, VI). Normal subjects used as controls were individuals with no history of dementia or other neurological disorders. Neuropathologic evaluation of control brains revealed only age-associated gross and histopathologic alterations (Braak and Braak NFT staging, I and SP stage, 0 or A). The subjects' demographic data are summarized in Table 1. The human studies were approved by Ethics Committees of TMIG and the Tokyo Metropolitan Geriatric Hospital.

Immunohistochemistry. Specimens were taken from the hippocampus and fixed with 4% paraformaldehyde in this study. Paraffin-embedded hippocampal sections were deparaffinized, rehydrated with xylene, alcohol and phosphate buffered saline (PBS), microwaved for 5 min in boiling 10 mM citrate buffer, pH 6.0, and immersed in 3% H_2O_2 in methanol for 15 min to reduce endogenous peroxidase activity. After blocking treatment with 10% non-immune goat serum in PBS (blocking solution) for 60 min at room temperature, the specimens were incubated with the primary antibodies overnight at 4°C and then for 60 min at room temperature. Mouse monoclonal antibody against HNE-histidine Michael adduct which was specific for their cyclic hemiacetal form was purchased from NOF Corporation (Tokyo,

Japan), and was used at a dilution of 1 : 100 with a blocking solution. After adequate washing with PBS, specimens were incubated with the secondary antibody (goat anti-mouse IgG conjugated with horseradish peroxidase, Simplestain MAX-PO (M); Nichirei Biosciences Inc., Tokyo, Japan) for 60 min at room temperature. Thorough washing with PBS and incubation with 0.02% 3,3'-diaminobenzidine tetrahydrochloride (DAB) (Wako Pure Chemical Industries, Osaka, Japan) followed for 10 min at room temperature to visualize HNE-adduct. For double-labeling immunohistochemistry, two primary antibodies were used: anti-microtubule-associated protein 2 (MAP2) and the anti-HNE-histidine adduct antibodies. Tissue specimens were incubated with the anti-MAP2 antibody (1 : 500 dilution; Chemicon AB5622, rabbit polyclonal antibody; Billerica, MA, USA) to confirm pyramidal neurons, and then with Simplestain AP (R) as a secondary antibody conjugated with alkaline phosphatase. The alkaline phosphatase activity was visualized with Vector Red Alkaline Phosphatase Substrate Kit I (Vector Laboratories, Burlingame, CA, USA). Subsequently, the specimens were incubated with the anti-HNE adduct antibody as mentioned above. Hematoxylin was used for counter staining. The antibody used against HNE-histidine Michael adduct is specific for their cyclic hemiacetal form and does not react with the ring-opened form of HNE-histidine Michael adduct and the pyrrole form of HNE-lysine Michael adduct (26).

The four hippocampal sectors (CA1 through CA4) were delineated and cells that had a large nucleus containing a clearly visible nucleolus in these sectors were referred to pyramidal cells according to the description of Mani *et al.* (14). Immunoreactive intensity of the HNE-Michael adduct was assessed by measuring 20 fields of hippocampal sectors in the specimens under a 40 × objective microscopic field. The extent of staining intensity in pyramidal cells was classified into the following two grades: Pyr-small (small staining size less than half of the pyramidal cell nucleus) and Pyr-large (large staining size more than half of the pyramidal cell nucleus). The extent of staining intensity in non-pyramidal cells was also classified into the following two grades: Non-small (small staining size less than the cell nuclei) and Non-large (large staining size more than the cell nuclei). The percent ratio of these grades in each sector was calculated by following formulation: percent of Pyr-small = (numbers of Pyr-small grade / (numbers of Pyr-small grade + Pyr-large grade)) × 100; percent of Pyr-large = (numbers of Pyr-large grade / (numbers of Pyr-small grade + Pyr-large grade)) × 100; percent of Non-small = (numbers of Non-small grade / (numbers of Non-small grade + Non-large grade)) × 100; and percent of Non-large = (numbers of Non-large grade / (numbers of Non-small grade + Non-large grade)) × 100.

Statistical analysis. The results are expressed as mean ± SEM. Statistical analyses were conducted by using Graphpad Prism 4 software (version 4.0, Graphpad Software Inc., San Diego, CA, USA). Significance was defined as a P value less than 0.05.

RESULTS

Clinical features of subjects

The subjects' demographic data are summarized in Table 1. The mean ages of the AD group and the control group were 86 and 78 years, respectively, and there was no significant difference between these two groups (*t-test*, two-sided). Neither brain weight, gender, nor postmortem interval differed significantly between the two groups according to a *t-test* (two-sided), Fisher's exact test, or *t-test* (two-sided), respectively.

HNE Michael adduct in the hippocampi from AD patients and non-AD controls

HNE Michael adduct in the hippocampi was detected in all specimens from both AD and controls. Especially, CA2–4 sectors contained an abundance of the HNE adduct compared with the adjacent CA1 sector (Fig. 1B and Table 2).

HNE Michael adduct immunoreactivity was seen

Table 1 *Demographic data for AD subjects and controls*

	Age (yr)	PMI (h)	Gender	BW (g)	Braak stage	
					NFT	SP
AD	86 ± 3	10.0 ± 0.1	2 M/2 F	1,110 ± 52	VI (4)	C (4)
Controls	78 ± 2	4.4 ± 2.5	3 M/1 F	1,241 ± 67	I (4)	0 (4)

Data are expressed as mean ± SEM. Parentheses indicate the number of subject. AD, Alzheimer disease; PMI, postmortem interval; h, hour; BW, brain weight; g, gram; yr, year; NFT, neurofibrillary tangle; SP, senile plaque

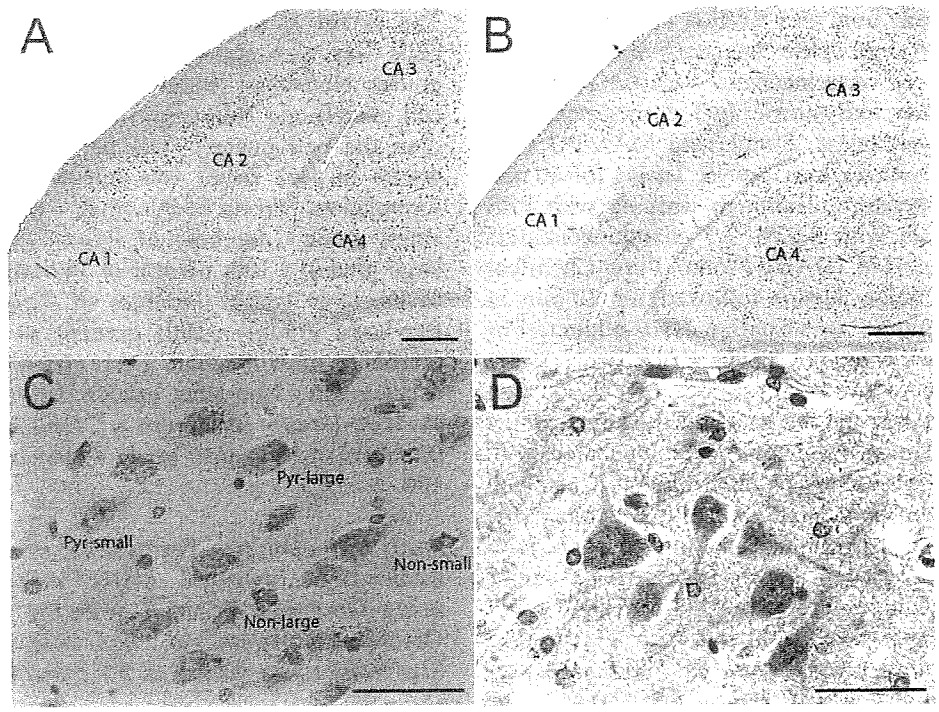

Fig. 1 Representative photomicrographs of immunostaining for HNE-Michael adduct in the hippocampus. HNE-Michael adduct in the hippocampi of AD (A, C, D) and non-AD control (B) and MAP2 (D) are visualized using DAB (brown) and Vector Red (pink), respectively. Counter staining was performed with hematoxylin. Substances with immunoreactivity to anti-HNE-histidine Michael adduct are seen in pyramidal cells as a granular form (C, D) and seen in non-pyramidal cells as amorphous deposits (C). For statistical analysis, the extent of staining intensity of the HNE adduct is classified into two grades (Pyr-small and Pyr-large) for the pyramidal cells, and two grades (Non-small and Non-large) for the non-pyramidal cells, as described in Materials and Methods. Bar = 50 μm (A and B) and 5 μm (C and D).

Table 2 *Immunostaining intensity of the HNE-Michael adduct in the hippocampus*

Sector	Case	Pyramidal cells			Non-pyramidal cells		
		Pyr-small	Pyr-large	*P* value	Non-small	Non-large	*P* value
CA1	AD	228	39		126	95	
	Control	433	25	< 0.0001	143	125	NS
CA2/3	AD	168	433		236	463	
	Control	296	425	< 0.0001	177	255	0.0157
CA4	AD	42	238		177	299	
	Control	206	364	< 0.0001	205	223	0.0012

Staining intensity of the HNE adduct is classified into two grades (Pyr-small and Pyr-large) for the pyramidal cells, and two grades (Non-small and Non-large) for the non-pyramidal cells, as described in Materials and Methods. Fisher's exact test; NS, not significant.

as intracellular accumulations within pyramidal cells in the hippocampi of AD and controls (indicated in brown in Fig. 1C and D). In addition to the criteria of pyramidal cells in Materials and Methods, pyramidal cells were also confirmed by anti-MAP2 antibody as shown in Fig. 1D. The HNE adduct seemed to be composed of a mass of granular substances localized in the perikarya of pyramidal cells in the hippocampus, especially at the CA2, CA3 and CA4 sectors (Fig. 1C and D). Notably, the staining intensity for HNE Michael adduct was far stronger in these sectors of the AD brain samples than in those of the controls (Table 2, Fisher's exact test: $P < 0.0001$). Similarly, the ratio of the severe grade indicated as Pyr-large was relatively higher in the CA2/3 and CA4 sectors of AD patients compared with controls (Fig. 2A).

Additionally, a large amount of amorphous HNE

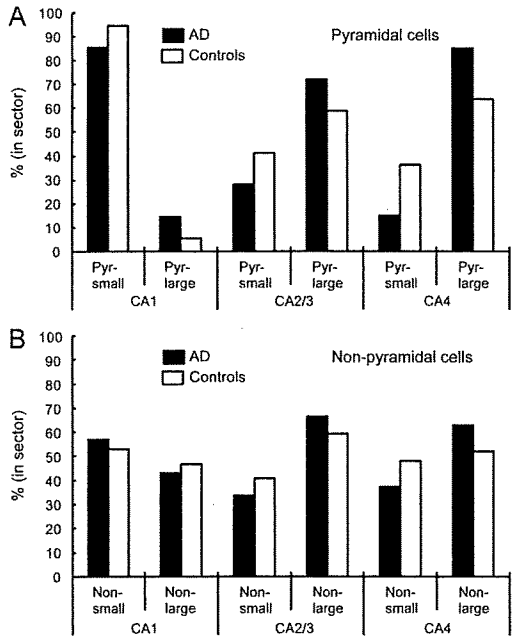

Fig. 2 Ratio of immunostaining intensity of the HNE-Michael adduct in the hippocampal sectors. Immunostaining intensity of the HNE-Michael adduct was assessed as described in Materials and Methods. Percent of the grades of HNE staining intensity in each sector was calculated as described in Materials and Methods. (A), pyramidal cells; (B), non-pyramidal cells; closed bars, AD; open bars, age-matched controls. The percent ratio of the Pyr-large grade of the pyramidal cells and the percent ratio of the Non-large grade of the non-pyramidal cells are relatively higher in the CA2/3 and CA4 sectors of AD patients compared with controls.

Michael adduct was seen around the nuclei of non-pyramidal cells other than the pyramidal cells in the hippocampus, and this material was referred to as non-pyramidal cell deposits (abbreviated as Non-small and Non-large in Fig. 1C). Numerous non-pyramidal cell deposits were found in the CA2, CA3 and CA4 sectors of the hippocampi from AD and controls (Table 2), but the staining intensity of these deposits again differed significantly in the two groups (Table 2, Fisher's exact test: $P < 0.02$). That is, the ratio of large amorphous deposits (Non-large grade in Table 2) to total deposits was relatively higher in these sectors of the AD tissue compared with that from age-matched controls (Fig. 2B).

DISCUSSION

Here, we found an intracellular accumulation of HNE-histidine Michael adduct in pyramidal cells of the hippocampus, most notably at the CA2, CA3 and CA4 sectors by using a specific antibody to cyclic hemiacetal type of HNE-histidine Michael adduct. This antibody does not react with the ring-opened form of HNE-histidine Michael adduct and the pyrrole form of HNE-lysine Michael adduct (26). Although the HNE adduct occupied hippocampi from both AD and age-matched, non-AD controls, significantly larger quantities of the HNE adduct were present in the CA2–4 sectors of AD patients than those of controls. These results show that pyramidal neurons in these sectors within hippocampi of persons with AD are prone to undergo lipid peroxidation. Consequently, increased lipid peroxidation might be responsible for the neuronal degeneration and death characteristic of AD. In support is the fact that HNE, a lipid peroxidation product is cytotoxic to cultured neuronal cells via impairment of Na^+, K^+-ATPase (15), disruptions of microtubule structure (7, 20), caspase-3 activation, and cytochrome c release (6).

The distribution of the HNE adduct differed among CA sectors in the hippocampus. Although a few pyramidal cells in the CA1 sector contained the HNE adduct, a great number of cells in the CA2–4 sectors contained massive amounts of the HNE adduct. A similar spatial distribution pattern was found for malondialdehyde-conjugated proteins identified in persons with AD and age-matched controls (4). Thus, these results suggest that pyramidal cells in the CA1 sector might resist lipid peroxidation. On the other hand, after sodium borohydride treatment, the ring-opened form of HNE-histidine Michael adduct was seen frequently in hippocampi of AD patients but rarely in age-matched controls, and in the former case the percentage of immunoreactive pyramidal cells in the CA1 sector was comparable to that of the CA2–4 sectors (19). That result disagrees with the outcome presented here, possibly because antibodies of differing specificities were used in the two studies. That is, the previously used antibody against the ring-opened form of HNE-histidine Michael adduct rarely stained hippocampi from control subjects, whereas the antibody used in this study stained hippocampal tissues from controls and AD patients to comparable extents.

We also showed that amorphous deposits immunoreactive to the anti-HNE adduct antibody in non-pyramidal cells were significantly increased in the CA2–4 sectors of hippocampal samples from AD patients compared with age-matched control. These deposits were found around small nuclei in the CA2–4 sectors of hippocampal samples. Although the all cell types containing these small nuclei were

not identified, some cells were positively stained with glial fibrillary acidic protein which is an astrocyte marker protein but not all cells. Immunoreactivity similar to the amorphous staining described here was seen in astrocytes when using antibody against the ring-opened form of HNE-histidine Michael adduct (19) and antibody against malondialdehyde-conjugated proteins (4). Therefore, the cells containing the small nuclei we viewed around amorphous deposits could be astrocytes.

In addition to the cyclic hemiacetal form and the ring-opened form of HNE-histidine Michael adduct, the pyrrole form of HNE-lysine Michael adduct (18, 24) was detected in the hippocampus (24) and entorhinal cortex (18) of samples from AD patients by using specific antibodies. Other than the immunohistochemical detection of HNE-conjugated proteins, elevated levels of HNE itself (17, 28) and isoprostanes (16, 22, 23), stable products derived from lipid peroxidation of PUFAs, these reports confirm increased lipid peroxidation in the brains of AD compared with control individuals. Thus, our results and those studies provide firm evidence of increased lipid peroxidation in brains that manifest AD.

Here we have documented strong evidence of lipid peroxidation in the hippocampi of both AD patients and age-matched, non-AD controls by identifying the presence of the HNE adduct. Presumably, the increased levels of HNE adduct in the hippocampi of AD patients signifies that the brains of such patients with AD tend to be more sensitive to lipid peroxidation than normal brains. In that environment, accelerated lipid peroxidation might play a pivotal role in the pathogenesis of AD by producing HNE and/or other cytotoxic products.

Acknowledgements

This study is supported by a Grant-in-Aid for Scientific Research from the Ministry of Education, Science, and Culture, Japan (to A.I., S.H. and N.S.) and a grant from Health Science Research Grants for Comprehensive Research on Aging and Health supported by the Ministry of Health Labor and Welfare, Japan (to A.I.). We thank Ms. Eiko Moriizumi for her technical advices on immunohistochemistry. We also thank Ms. P. Minick for the excellent English editorial assistance.

REFERENCES

1. Consensus recommendations for the postmortem diagnosis of Alzheimer's disease (1997). The National Institute on Aging, and Reagan Institute Working Group on Diagnostic Criteria for the Neuropathological Assessment of Alzheimer's Disease. *Neurobiol Aging* **18**, S1–2.
2. Abdul HM and Butterfield DA (2007) Involvement of PI3K/PKG/ERK1/2 signaling pathways in cortical neurons to trigger protection by cotreatment of acetyl-L-carnitine and alpha-lipoic acid against HNE-mediated oxidative stress and neurotoxicity: implications for Alzheimer's disease. *Free Radic Biol Med* **42**, 371–384.
3. Amarnath V, Valentine WM, Montine TJ, Patterson WH, Amarnath K, Bassett CN and Graham DG (1998) Reactions of 4-hydroxy-2(E)-nonenal and related aldehydes with proteins studied by carbon-13 nuclear magnetic resonance spectroscopy. *Chem Res Toxicol* **11**, 317–328.
4. Dei R, Takeda A, Niwa H, Li M, Nakagomi Y, Watanabe M, Inagaki T, Washimi Y, Yasuda Y, Horie K, Miyata T and Sobue G (2002) Lipid peroxidation and advanced glycation end products in the brain in normal aging and in Alzheimer's disease. *Acta Neuropathol* **104**, 113–122.
5. Esterbauer H, Schaur RJ and Zollner H (1991) Chemistry and biochemistry of 4-hydroxynonenal, malonaldehyde and related aldehydes. *Free Radic Biol Med* **11**, 81–128.
6. Ji C, Amarnath V, Pietenpol JA and Marnett LJ (2001) 4-hydroxynonenal induces apoptosis via caspase-3 activation and cytochrome c release. *Chem Res Toxicol* **14**, 1090–1096.
7. Kokubo J, Nagatani N, Hiroki K, Kuroiwa K, Watanabe N and Arai T (2008) Mechanism of destruction of microtubule structures by 4-hydroxy-2-nonenal. *Cell Struct Funct* **33**, 51–59.
8. Kruman I, Bruce-Keller AJ, Bredesen D, Waeg G and Mattson MP (1997) Evidence that 4-hydroxynonenal mediates oxidative stress-induced neuronal apoptosis. *J Neurosci* **17**, 5089–5100.
9. Liu X, Lovell MA and Lynn BC (2005) Development of a method for quantification of acrolein-deoxyguanosine adducts in DNA using isotope dilution-capillary LC/MS/MS and its application to human brain tissue. *Anal Chem* **77**, 5982–5989.
10. Lovell MA, Ehmann WD, Butler SM and Markesbery WR (1995) Elevated thiobarbituric acid-reactive substances and antioxidant enzyme activity in the brain in Alzheimer's disease. *Neurology* **45**, 1594–1601.
11. Lovell MA and Markesbery WR (2007) Oxidative damage in mild cognitive impairment and early Alzheimer's disease. *J Neurosci Res* **85**, 3036–3040.
12. Lovell MA, Xie C and Markesbery WR (2001) Acrolein is increased in Alzheimer's disease brain and is toxic to primary hippocampal cultures. *Neurobiol Aging* **22**, 187–194.
13. Mamelak M (2007) Alzheimer' s disease, oxidative stress and gammahydroxybutyrate. *Neurobiol Aging* **28**, 1340–1360.
14. Mani RB, Lohr JB and Jeste DV (1986) Hippocampal pyramidal cells and aging in the human: a quantitative study of neuronal loss in sectors CA1 to CA4. *Exp Neurol* **94**, 29–40.
15. Mark RJ, Lovell MA, Markesbery WR, Uchida K and Mattson MP (1997) A role for 4-hydroxynonenal, an aldehydic product of lipid peroxidation, in disruption of ion homeostasis and neuronal death induced by amyloid beta-peptide. *J Neurochem* **68**, 255–264.
16. Markesbery WR, Kryscio RJ, Lovell MA and Morrow JD (2005) Lipid peroxidation is an early event in the brain in amnestic mild cognitive impairment. *Ann Neurol* **58**, 730–735.
17. Markesbery WR and Lovell MA (1998) Four-hydroxynonenal, a product of lipid peroxidation, is increased in the brain in Alzheimer's disease. *Neurobiol Aging* **19**, 33–36.

18. Montine KS, Olson SJ, Amarnath V, Whetsell WO, Jr., Graham DG and Montine TJ (1997) Immunohistochemical detection of 4-hydroxy-2-nonenal adducts in Alzheimer's disease is associated with inheritance of APOE4. *Am J Pathol* **150**, 437–443.
19. Montine KS, Reich E, Neely MD, Sidell KR, Olson SJ, Markesbery WR and Montine TJ (1998) Distribution of reducible 4-hydroxynonenal adduct immunoreactivity in Alzheimer disease is associated with APOE genotype. *J Neuropathol Exp Neurol* **57**, 415–425.
20. Neely MD, Sidell KR, Graham DG and Montine TJ (1999) The lipid peroxidation product 4-hydroxynonenal inhibits neurite outgrowth, disrupts neuronal microtubules, and modifies cellular tubulin. *J Neurochem* **72**, 2323–2333.
21. Porter NA, Caldwell SE and Mills KA (1995) Mechanisms of free radical oxidation of unsaturated lipids. *Lipids* **30**, 277–290.
22. Pratico D, V MYL, Trojanowski JQ, Rokach J and Fitzgerald GA (1998) Increased F2-isoprostanes in Alzheimer's disease: evidence for enhanced lipid peroxidation in vivo. *FASEB J* **12**, 1777–1783.
23. Reich EE, Markesbery WR, Roberts LJ, 2nd, Swift LL, Morrow JD and Montine TJ (2001) Brain regional quantification of F-ring and D-/E-ring isoprostanes and neuroprostanes in Alzheimer's disease. *Am J Pathol* **158**, 293–297.
24. Sayre LM, Zelasko DA, Harris PL, Perry G, Salomon RG and Smith MA (1997) 4-Hydroxynonenal-derived advanced lipid peroxidation end products are increased in Alzheimer's disease. *J Neurochem* **68**, 2092–2097.
25. Smith MA (1998) Alzheimer disease. *Int Rev Neurobiol* **42**, 1–54.
26. Tanaka T, Nishiyama Y, Okada K, Hirota K, Matsui M, Yodoi J, Hiai H and Toyokuni S (1997) Induction and nuclear translocation of thioredoxin by oxidative damage in the mouse kidney: independence of tubular necrosis and sulfhydryl depletion. *Lab Invest* **77**, 145–155.
27. Uchida K and Stadtman ER (1992) Modification of histidine residues in proteins by reaction with 4-hydroxynonenal. *Proc Natl Acad Sci USA* **89**, 4544–4548.
28. Williams TI, Lynn BC, Markesbery WR and Lovell MA (2006) Increased levels of 4-hydroxynonenal and acrolein, neurotoxic markers of lipid peroxidation, in the brain in Mild Cognitive Impairment and early Alzheimer's disease. *Neurobiol Aging* **27**, 1094–1099.
29. Xiao Y, Huang Y and Chen ZY (2005) Distribution, depletion and recovery of docosahexaenoic acid are region-specific in rat brain. *Br J Nutr* **94**, 544–550.

ORIGINAL RESEARCH

A.M. Tokumaru
Y. Saito
S. Murayama
K. Kazutomi
Y. Sakiyama
M. Toyoda
M. Yamakawa
H. Terada

Imaging-Pathologic Correlation in Corticobasal Degeneration

BACKGROUND AND PURPOSE: The clinical diagnosis of corticobasal degeneration (CBD) is often difficult due to varied clinical manifestations. In 4 patients with neuropathologically confirmed CBD, characteristic imaging findings and correlations with neuropathologic features were evaluated. Furthermore, imaging findings in CBD were compared with neuropathologically confirmed progressive supranuclear palsy (PSP) for a differential diagnosis.

MATERIALS AND METHODS: Four patients with neuropathologically confirmed CBD were studied. We evaluated the area of the tegmentum in the midsagittal plane, subcortical white matter (SCWM) abnormality, asymmetric cerebral atrophy, and signal-intensity abnormality in the subthalamic nuclei on MR imaging and compared them with histopathologic findings. Then, MR imaging findings in CBD were compared with those in 13 patients with PSP.

RESULTS: On MR imaging, 3 patients had asymmetric cerebral atrophy extending to the central sulcus. On midsagittal sections, the mean midbrain tegmentum area was 66 mm^2, being markedly smaller than normal, but there was no significant difference between PSP and CBD. All patients had signal-intensity abnormalities of the SCWM, constituting primary degeneration neuropathologically; however, no diffuse signal-intensity abnormality in the SCWM existed in the 13 patients with PSP. In 3 patients, T1-weighted images showed symmetric high signal intensity in the subthalamic nuclei. Neuropathologically, these areas showed characteristic CBD. MR imaging signal-intensity changes also existed in 4 patients with PSP; however, subthalamic nucleus degeneration was more severe in PSP than in CBD.

CONCLUSIONS: In cases with midbrain tegmentum atrophy and signal-intensity changes in the subthalamic nuclei, the differential diagnosis distinguishing CBD from PSP based on MR imaging alone was difficult. White matter lesions and asymmetric atrophy can be useful for a differential diagnosis.

Corticobasal degeneration (CBD) is a slowly progressive disorder with a clinically asymmetric onset characterized by apraxia, dystonia, postural instability, and an akinetic-rigid syndrome that does not respond to levodopa. However, clinical phenotypes of Alzheimer disease, Pick disease, and progressive supranuclear palsy (PSP) with similar characteristic features often make a differential diagnosis distinguishing these entities from CBD difficult in clinical practice.

Koyama et al[1] recently reported asymmetric cerebral atrophy with dominance contralateral to the more clinically affected side, hyperintensity in the subcortical white matter (SCWM) in the frontotemporal area on fluid-attenuated inversion recovery (FLAIR), and atrophy of the midbrain tegmentum as new imaging findings of clinically diagnosed CBD, but no imaging findings in pathologically proved cases have been reported.[3,4] We encountered 4 patients with neuropathologically confirmed CBD in whom the findings could be compared with those of MR imaging. Cortical symptoms were unclear in 3, and it was difficult to make a diagnosis on the basis of clinical symptoms alone because of underlying dementia. Although the number of cases was small, because the neuropathology and images were collated in all cases, this study was significant with regard to the objectivity of the imaging findings associated with an accurate diagnosis. We also thought that it was important to identify differences in imaging findings between CBD and PSP, in which severe atrophy of the midbrain tegmentum has been reported.[1,2] Therefore, MR imaging findings in CBD were compared with those in 13 cases of neuropathologically confirmed PSP.

Received January 3, 2009; accepted after revision May 12.

From the Departments of Diagnostic Radiology (A.M.T., M.T., M.Y.), Neuropathology (S.M.), and Neurology (K.K.), Tokyo Metropolitan Medical Center of Gerontology, Itabashi-Ku, Tokyo, Japan; Department of Neuropathology (Y. Saito), National Center of Neurology and Psychiatry, Kodaira, Tokyo, Japan; Department of Neurology (Y. Sakiyama), Jichi Medical College, Omiya, Saitama, Japan; and Department of Radiology (H.T.), Toho University, Sakura Medical Center, Sakura, Chiba, Japan.

Please address correspondence to Aya M. Tokumaru, MD, PhD, Department of Radiology, Tokyo Metropolitan Medical Center of Gerontology, 35-2 Sakaecho, Itabashi-ku, Tokyo 173-0015, Japan; e-mail: tokumaru@tmghig.jp

DOI 10.3174/ajnr.A1721

Materials and Methods

Patients

Four patients (1 man, 3 women) with neuropathologically confirmed CBD were evaluated retrospectively. The patients' mean age at death was 70.8 years (range, 67–74 years). Table 1 lists the patient characteristics. The MR imaging findings in the patients with CBD (Table 2) were compared with those in 13 patients with neuropathologically confirmed PSP. All 13 patients with PSP were men, with a mean age at death of 78.3 years (range, 64–87 years). For the comparative evaluation of atrophy of the midbrain tegmentum, 10 aged-matched control subjects (4 men and 6 women) with no neuropathologic degenerative disease or cerebrovascular disorder were selected (mean age at death, 74.6 years; range, 68–83 years).

MR Imaging Examinations

All studies were performed with a 1.5T MR imaging unit (Signa Excite HD; GE Healthcare, Milwaukee, Wis). Axial T2-weighted images (TR/TE, 4300/89 ms; NEX, 2; FOV, 220 mm; section thickness, 5 mm with a section gap of 1 mm) and FLAIR images (TR/TE, 10,002/106 ms; TI, 2500 ms; NEX, 1; section thickness, 5 mm with a gap of 1 mm), sagittal T1-weighted images (TR/TE, 600/14 ms; NEX, 2; section thickness, 5 mm with a gap of 1 mm), or sagittal spoiled gradient-echo

Table 1: Clinical findings of pathologically confirmed corticobasal degeneration

Case No.	Age at Onset (yr)	Sex	Duration (yr)	Rigidity	Dystonia	Pyramidal Signs	Cortical Dysfunction	Vertical Gaze Palsy	Dementia	CDx
1	74	F	10	Lt>Rt	–	–	Ocular apraxia	+	Mute	PSP?
2	68	F	6	Lt>Rt			Apraxia (Lt hand)	±	+ Severe akinetic mute	AD
3	67	M	3	Rt>Lt			No cortical sign	+	+ Severe	PDD
4	74	F	6	Rt>Lt	–	–	–	+	+ Severe	CBD

Note:—CBD indicates corticobasal degeneration; PSP?, progressive supranuclear palsy suspected; CDx, clinical diagnosis; AD, Alzheimer disease; PDD, Parkinson disease with dementia; –, no symptom; +, obvious symptom; ±, suspicious symptom; Lt, left; Rt, right.

Table 2: MR imaging findings of neuropathologically confirmed corticobasal degeneration

Case No.	Atrophy (Dominant Cerebral Hemisphere)	White Matter Hyperintensity on FLAIR: Precentral Gyrus	White Matter Hyperintensity on FLAIR: Frontal Lobe	Hyperintensity on T1WI in Bil Subthalamic Nucleus
1	Rt frontal operculum and convexity	–	+	+
2	Bil frontal convexity	–	+	+
3	Lt frontoparietal	Bil	+	+
4	Rt frontoparietal	Rt	+	+

Note:—FLAIR indicates fluid-attenuated inversion recovery; T1WI = T1-weighted imaging; Bil, bilateral; –, no signal abnormality; +, obvious signal abnormality.

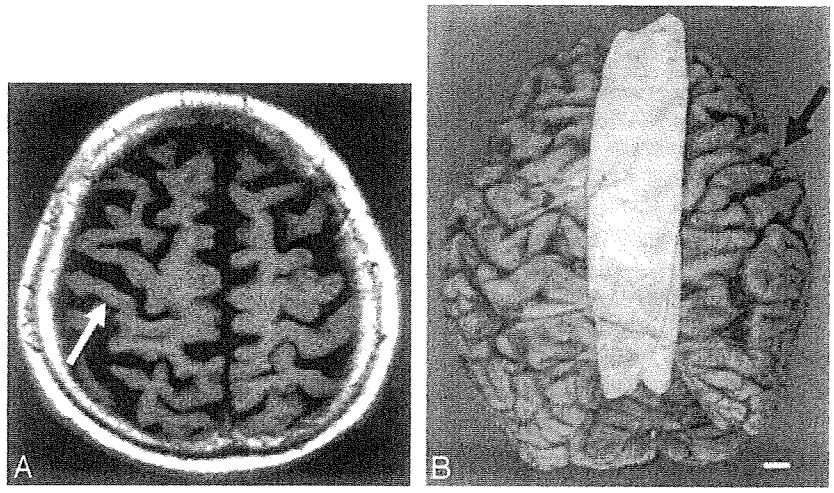

Fig 1. Corticobasal degeneration, case 1. An 84-year-old woman. *A*, Axial T2-weighted image shows right-side-dominant atrophy including the central sulcus (*arrow*). *B*, A macrospecimen of this patient shows right-frontal-dominant atrophy (*arrow*).

images (TR/TE, 21/6 ms; TI, 0 ms; flip angle, 20°) were obtained in all patients with CBD and PSP and healthy controls. Spin-echo coronal T1-weighted images (TR/TE, 600/14 ms; NEX, 2; section thickness, 5 mm with a gap of 1 mm) were obtained in 3 of the 4 patients with CBD, 7 of the 13 patients with PSP, and the 10 age-matched healthy controls. In 1 patient with CBD and 3 with PSP, T1-weighted coronal spin-echo images could not be obtained; spoiled gradient-echo imaging (TR/TE, 21/6 ms; TI, 0 ms; flip angle, 20°) was selected instead. These patients and 3 other patients with PSP without coronal sections were excluded from evaluation of the T1-weighted signal intensity. The area of the midbrain tegmentum was measured on an MR imaging workstation by using the method of Oba et al[2] in a T1-weighted midsagittal section through the center of the interpeduncular cistern and the center of the cerebral aqueduct. Two neuroradiologists (A.M.T. and M.T.) performed these measurements blindly, twice at different times.

The localization and laterality of cerebral atrophy, signal intensity in the subthalamic nuclei, and signals in the SCWM were only qualitatively investigated because of the limitations of the retrospective nature of pathologically confirmed cases. The 2 neuroradiologists blindly investigated images of 4 patients with CBD, 13 patients with PSP, and 10 healthy controls twice at different times and visually evaluated the following points: 1) the presence or absence and laterality of cerebral atrophy and whether the atrophy included the central sulcus on T1-weighted imaging, 2) the presence or absence and localization of a high signal intensity in the SCWM on T2-weighted or FLAIR imaging, and 3) the presence or absence of an increase in the signal intensity in the subthalamic nuclei in the coronary view on T1-weighted imaging.

Neuropathologic Examinations

Informed consent for autopsy was obtained from all of the patients or their families. All serial autopsy cases were examined with the Brain Bank Aging Research protocol, irrespective of clinical diagnosis.[3] At autopsy, after taking photographs of the whole brain, we serially sectioned the nondominant hemisphere or the hemisphere spared from focal lesions at a 7-mm thickness. The cerebrum was cut on the coronal plane; the brain stem, on the axial plane; and the cerebellum, on

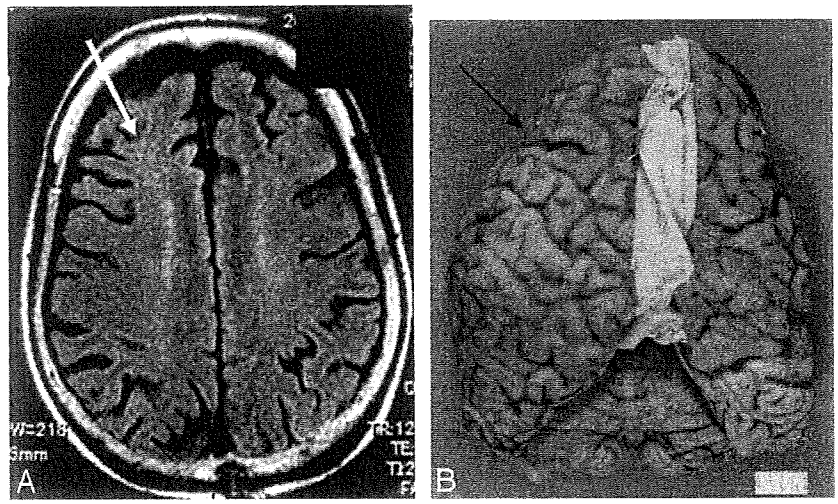

Fig 2. Corticobasal degeneration, case 2. A 74-year-old woman. *A*, An axial fluid-attenuated inversion recovery image 3 years before autopsy shows no obvious asymmetric atrophy. Subcortical hyperintensity is shown in the right frontal white matter (*white arrow*). *B*, A macrospecimen of this patient shows mild frontal atrophy with some asymmetry (*arrow*).

the sagittal plane. Photographs were taken of all sections. Small pieces of the anterior amygdala; posterior hippocampus; frontal, temporal, and occipital poles; supramarginal gyrus; and rostral midbrain were directly fixed in 4% paraformaldehyde for 48 hours and prepared for immunohistochemical and ultrastructural studies. The remaining sections were quick frozen and stored at −80°C. The hemisphere kept for morphologic examinations was fixed in 20% neutral buffered formalin for 7–13 days and cut into 7-mm-thick sections, similar to those in the contralateral hemisphere. Paraffin-embedded sections of representative areas of the brain were examined.

The selected anatomic structures included those recommended by the Consortium to Establish a Registry for Alzheimer Disease,[4] the Consensus Guidelines for the Diagnosis of Dementia with Lewy Bodies,[5,6] Braak and Braak's recommendation,[7] and the Diagnostic Criteria of Corticobasal Degeneration and Progressive Supranuclear Palsy.[8,9] These included the frontal pole; temporal pole; cingulate gyrus; second frontal gyrus; accumbens and septal nuclei; amygdala; basal nucleus of Meynert; second temporal gyrus; anterior hippocampus with entorhinal and transentorhinal cortices; basal ganglia and hypothalamus with mamillary bodies; subthalamic nucleus; posterior hippocampus; thalamus with the red nucleus; motor cortex; parietal lobe with the intraparietal sulcus; visual cortex; midbrain; upper and middle pons; medulla oblongata; cerebellar vermis; dentate nucleus; and multiple cervical, thoracic, and lumbar levels of the spinal cord.

Six-micrometer-thick sections were routinely stained with hematoxylin-eosin and the Klüver-Barrera method. Selected sections were stained with the modified methenamine, Gallyas-Braak, and Bielschowsky silver staining for age-related changes, with Congo red for amyloid β deposition and elastica-Masson trichrome staining for vascular changes.

Immunohistochemistry

Six-micrometer-thick serial sections were immunohistochemically stained by using a 20NX autostainer (Ventana, Tucson, Ariz), as previously described. The antibodies applied to all the cases were the following: antiphosphorylated α-synuclein (psyn); phosphorylated tau (ptau) (AT8, monoclonal; Innogenetic, Temse, Belgium); 3-repeat tau (RD3, amino acids 209–224, monoclonal, Upstate; Millipore, Lake Placid, NY); 4-repeat tau (RD4, amino acid 275–291, monoclonal, Upstate; Millipore); amyloid β 11–28 (12B2, monoclonal; IBL, Maebashi, Japan); glial fibrillary acidic protein (polyclonal; DAKO, Glostrup, Denmark); HLA-DR (monoclonal, CD68; DAKO); phosphorylated neurofilament (monoclonal SMI31; Sternberger Immunochemical, Baltimore, Md); myelin basic proteins (polyclonal, DAKO); and ubiquitin (polyclonal, DAKO) antibodies.

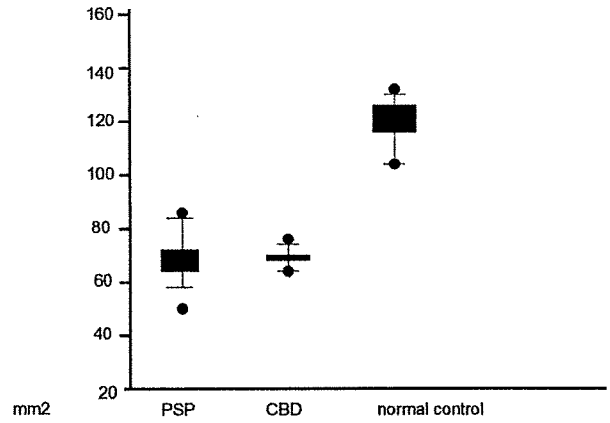

Fig 3. Scatterplot (mean, SD, and range) of the area of the midbrain in patients with progressive supranuclear palsy (PSP), corticobasal degeneration (CBD), and age-matched healthy controls. There was no individual overlap of the midbrain tegmental area between the healthy controls and patients with CBD and PSP, apparently showing that severe atrophy of the midbrain tegmentum was present in patients with CBD and PSP.

In addition to the routine neuropathologic examination mentioned above, studies were performed at sites of MR imaging signal-intensity abnormalities or atrophy to correlate the radiologic and pathologic findings. To compare them with MR imaging findings, 2 neuropathologists investigated the following points in addition to routine examinations: 1) the macroscopic presence or absence, laterality, and localization of cerebral atrophy at the time of sectioning the brain and after fixation, 2) the macroscopic presence or absence of atrophy of the midbrain tegmentum at the time of sectioning the brain and after fixation, 3) the presence or absence and degree of degeneration of the subthalamic nuclei, and 4) the presence or absence of a lesion in the SCWM and whether the lesion constituted primary or secondary degeneration in CBD. For brain samples, 7-mm coronal sections of the lateral region passing the mamillary body vertical to the hippocampal structure were prepared. Abnormal intensi-

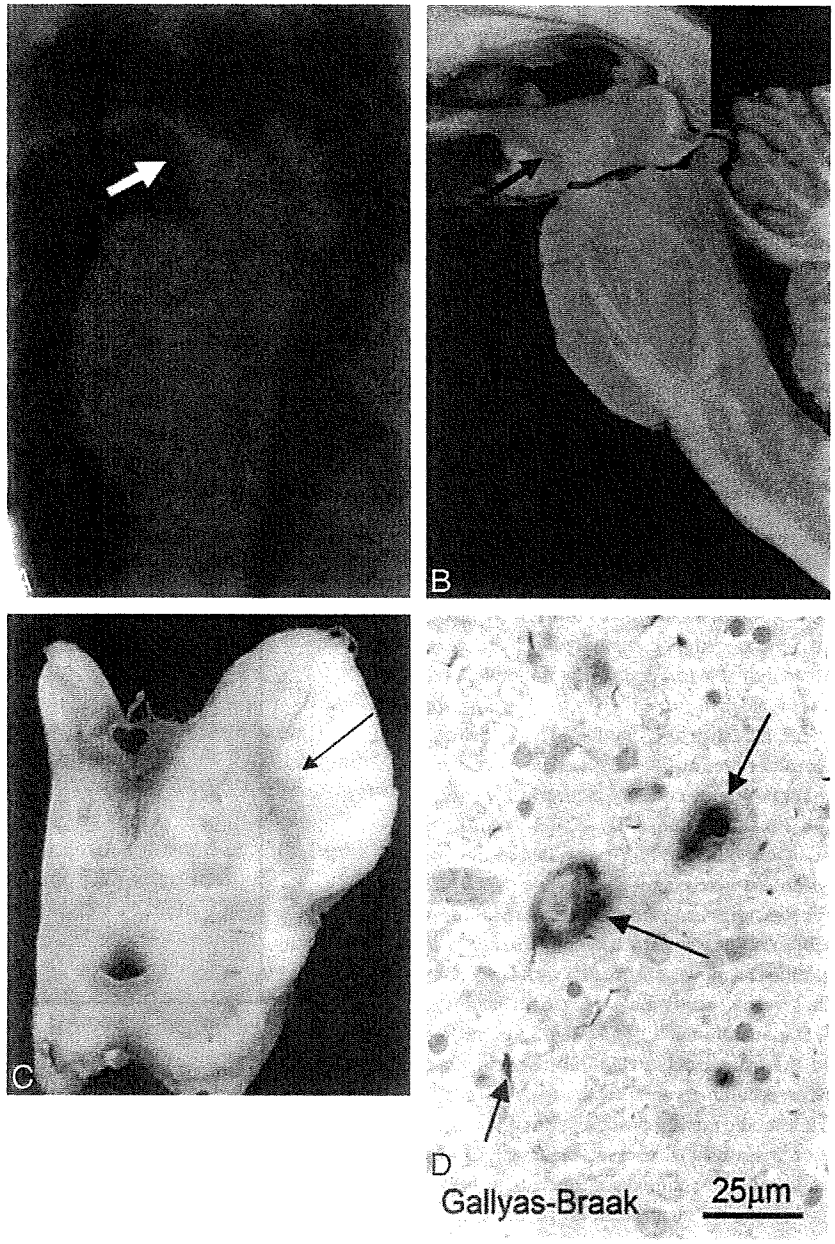

Fig 4. Corticobasal degeneration (CBD), case 1. An 84-year-old woman. *A*, T1-weighted midsagittal image clearly shows atrophy of the midbrain tegmentum (*arrow*). The area of the midbrain tegmentum is 73 mm^2. *B*, A macroscopic specimen of the midbrain shows marked atrophy (*arrow*). *C*, A macroscopic view of the midbrain shows discoloration of the substantia nigra (*arrow*). *D*, A microscopic view of the substantia nigra (Gallyas-Braak stain) shows argyrophilic threads and granular or fibrous inclusion bodies (*arrows*). These are consistent with CBD.

ties on MR imaging were collated with the pathologic preparations as accurately as possible, with the line passing the mamillary body vertical to the hippocampal structure as the baseline, and new pathologic sections were cut out as needed.

Results

Asymmetric Cerebral Atrophy

Asymmetric cerebral atrophy was observed in 3 of 4 patients with predominance contralateral to the more clinically affected side. In all 3 patients, cerebral atrophy affected the area including the central sulcus. In 1 patient, the radiologic and pathologic findings of predominantly frontal lobe atrophy were correlated (case 1, Fig 1*A*, -*B*). In 1 patient (case 2, Fig 2*A*, -*B*) in whom the interval between MR imaging and autopsy was 3 years, asymmetric cortical atrophy was difficult to detect on MR imaging, but frontal atrophy with some asymmetry was seen on autopsy. In this patient, clinical evaluation revealed no asymmetric cortical symptoms, so the clinical diagnosis was Alzheimer disease. In the 13 cases with PSP, excluding 1 patient, no asymmetric atrophy was noted.

Atrophy of Midbrain Tegmentum

On midsagittal sections, by using the method of Oba et al,[2] the mean area of the midbrain tegmentum of the 4 patients with CBD was 67.6 ± 7.4 mm^2 (range, 62.3–73.3 mm^2) (Fig 3; case 1, Fig 4*A*–*D*), which is markedly less than normal, with the

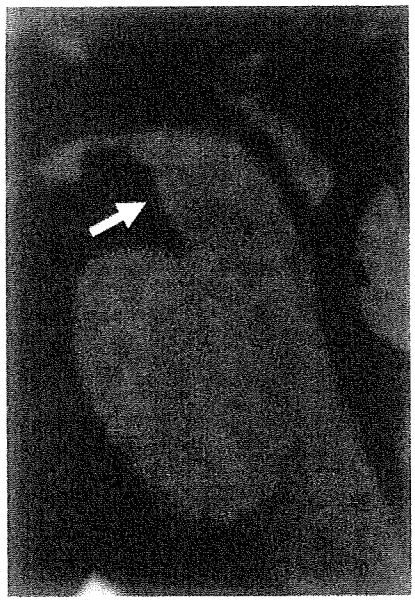

Fig 5. An age-matched healthy control 72-year-old woman. T1-weighted midsagittal image shows no obvious atrophy of the midbrain tegmentum (*arrow*). The area of the midbrain tegmentum is 128 mm^2.

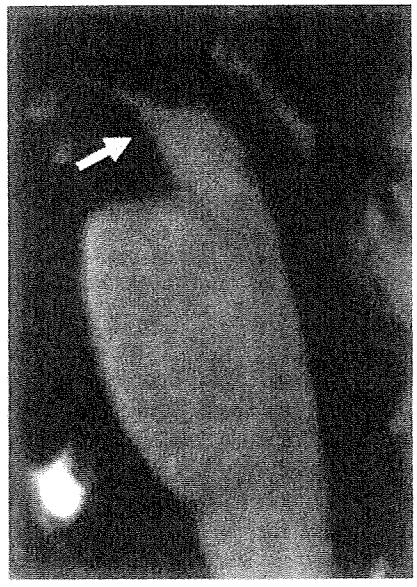

Fig 6. Progressive supranuclear palsy. A 74-year-old man. T1-weighted midsagittal image clearly shows atrophy of the midbrain tegmentum (*arrow*). The area of the midbrain tegmentum is 71 mm^2.

mean area of 123.8 ± 10.8 mm^2 in the controls (range, 108.0–132.4 mm^2) (Figs 3 and 5). In the 13 patients with neuropathologically confirmed PSP, the mean area was 70.7 ± 12.1 mm^2 (range, 58.6–89.8 mm^2) (Figs 3 and 6). Although statistical analysis was not possible because of the small number of cases, there was no individual overlap of the midbrain tegmental area between the healthy controls and patients with CBD and PSP, apparently showing that severe atrophy of the midbrain tegmentum was present in CBD and PSP. On neuropathologic examination, there was also atrophy of the midbrain tegmentum and marked depigmentation of the substantia nigra and locus ceruleus. Other findings included melanophagia and gliosis, and Gallyas-Braak silver staining revealed argyrophilic threads and granular or fibrous inclusion bodies. These findings were consistent with CBD. In the pontine tegmentum and oculomotor and trochlear nuclei, many AT8-immunoreactive pretangles were observed.

SCWM Signa-Intensity Change on T2-Weighted Images and FLAIR

In all 4 patients with CBD, T2-weighted images and FLAIR showed diffuse high-intensity signals in the SCWM. In 3 patients, high signal intensity in the SCWM was recognized on the predominantly atrophic side (case 1, Fig 7*A*–*C*). In 1 patient, a high signal intensity was noted bilaterally over a wide area in the frontal lobes (case 3, Fig. 8*A*–*C*). Corresponding to the sites of white matter lesions, myelin sheath staining was decreased, and these sites were stained positively for antiphosphorylated tau antibody. These changes are primary characteristic of CBD. On neuropathologic examination, there was some involvement of U-fibers, but because of image-quality limitations on MR imaging, U-fiber involvement could not be specifically detected. In the 13 patients with PSP, there was no diffuse signal-intensity abnormality in the SCWM. There was no neuropathologic finding indicating primary degeneration of the SCWM.

Symmetric High Signal Intensity Bilaterally in Subthalamic Nuclei on T1-Weighted Images

T1-weighted MR images showed symmetric high signal intensity bilaterally in the subthalamic nuclei in all 3 patients in whom T1-weighted images were obtained (case 1, Fig 9*A*–*C*). In the remaining patient, the signal intensity in the subthalamic nuclei was not evaluated because no T1-weighted coronal spin-echo images could be obtained. Spoiled gradient echo (TR/TE, 21/6 ms; TI, 0 ms; flip angle, 20°) was selected instead. These sites showed a brownish change on macroscopic examination, and on microscopic examination, antiphosphorylated tau antibody–positive neurons and gliosis were observed. These changes were characteristic of CBD. MR imaging signal-intensity changes were also present in 4 of 7 patients with PSP in whom T1-weighted images were obtained (Fig 10*A*–*C*). Because neuropathologically examined cases were retrospectively evaluated, signal-intensity evaluation was limited to visual examination by 2 neuroradiologists. It was difficult to distinguish CBD and PSP on imaging, and no asymmetry was identified. However, on neuropathologic examination, degeneration of the subthalamic nuclei was more severe in PSP than in CBD.

Discussion

In 3 of the 4 patients with CBD, atrophy was predominantly contralateral and extended to the central sulcus. On neuropathologic examination, the MR imaging findings of atrophy were confirmed. In 1 patient with no asymmetric cortical symptoms, there was no asymmetry on MR imaging (case 2, Fig 3*A*, -*B*) and the clinical diagnosis was Alzheimer disease. In this patient, in whom the interval between the last MR imaging and autopsy was 3 years, neuropathologic examination did show asymmetric atrophy, but it was mild compared with that in the other 3 patients. In some patients, CBD presents with dementia, behavioral abnormalities, and attention deficit in

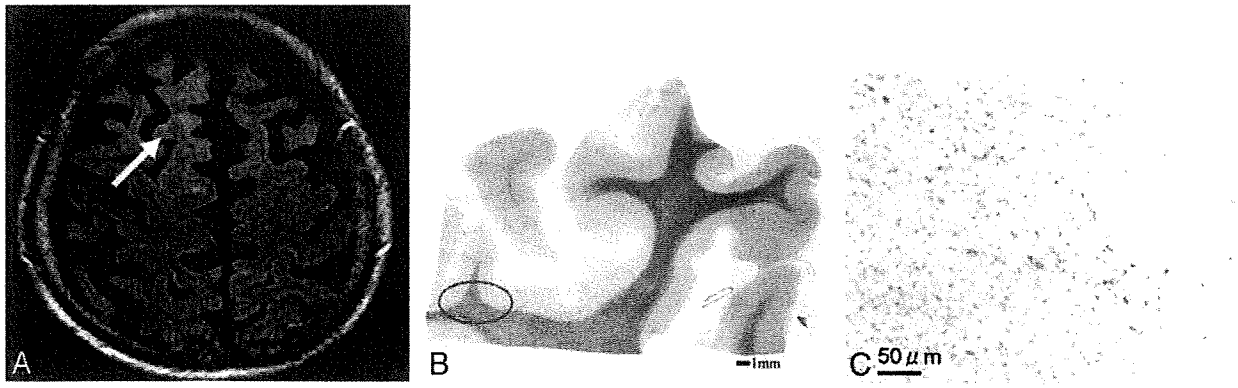

Fig 7. Corticobasal degeneration (CBD), case 1. An 84-year-old woman. *A*, Axial T2-weighted image shows a high signal intensity in the right frontal subcortical white matter (*white arrow*). *B*, In a microscopic specimen of the right frontal lobe corresponding to the site of white matter lesions, myelin sheath staining is decreased (*red oval*). The scale is 1 mm. *C*, In this area, there is positive staining for antiphosphorylated tau antibody on AT8 staining, which is compatible with the primary changes in CBD. The scale is 50 μm.

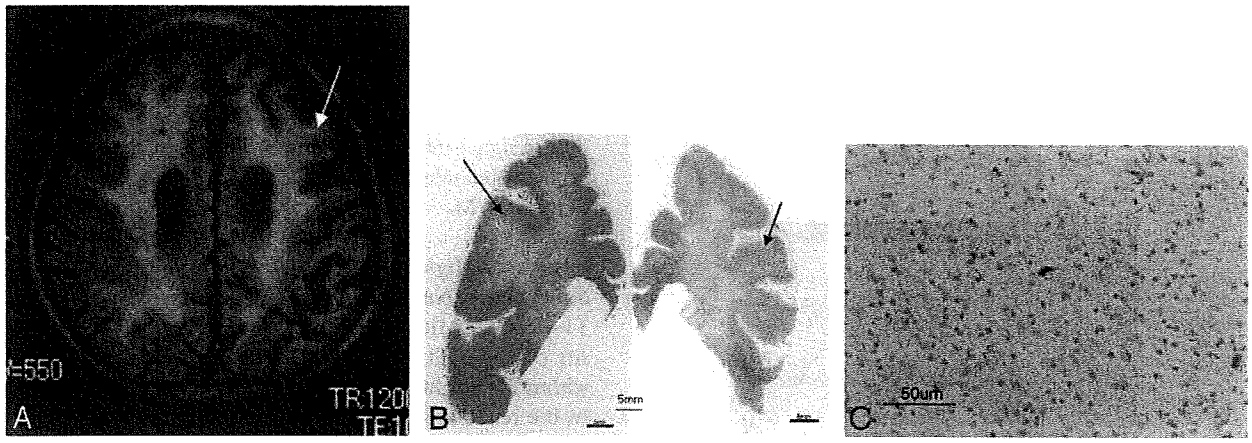

Fig 8. Corticobasal degeneration (CBD), case 3. A 70-year-old man. *A*, An axial fluid-attenuated inversion recovery image shows a high signal intensity bilaterally over a wide area in the frontal lobes (*arrow*). *B*, Corresponding to sites of white matter lesions, myelin sheath staining is decreased (*arrow*). The scale is 5 mm. *C*, These sites are stained positively for antiphosphorylated tau antibody. The scale is 50 μm. The changes are primary characteristics of CBD.

the early stage, but patients may be misdiagnosed due to a lack of cortical symptoms.[10-14] The above patient (case 2) may be an example of such a clinical presentation. Clinical evaluation showed little evidence of asymmetric cortical dysfunction, and neuropathology revealed only minimal cortical asymmetry. In this case, MR imaging showed a slight high signal intensity in the frontal SCWM; the midbrain tegmentum was severely atrophied, with an area of 71 mm^2; and T1-weighted imaging showed symmetric high-intensity signals in the subthalamic nucleus. Although a clear description is difficult on the basis of only 1 case, it was demonstrated by the pathologic findings that when identification of the cortical sign is difficult and unilateral atrophy is unclear on imaging, imaging findings, such as atrophy of the midbrain tegmentum, an abnormal signal intensity in the SCWM on FLAIR, or signal intensity changes in the subthalamic nuclei on T1-weighted imaging, may serve as supportive findings suggesting CBD.

CBD is important to differentiate from PSP. Oba et al[2] described a convenient and objective approach to diagnosing PSP based on midsagittal measurement of the midbrain tegmentum area. However, Koyama et al[1] also reported midbrain tegmentum atrophy in CBD. In our 4 cases of neuropathologically confirmed disease, severe midbrain tegmentum atrophy was also observed. Although there was a limited number of cases, because there was no individual overlap of the midbrain tegmental area between the healthy controls and patients with pathologically confirmed CBD and PSP, investigation of midbrain tegmental atrophy may have led to the diagnosis of CBD and PSP. Although no statistical analysis was performed because of the limited number of cases, it may be difficult to differentiate CBD from PSP on the basis of the presence of midbrain tegmental atrophy alone. A so-called "penguin sign" may be a distinguishing feature of PSP, but with severe midbrain tegmentum atrophy, both PSP and CBD must be considered. On neuropathology, there was marked depigmentation of the substantia nigra and locus ceruleus. Other findings included melanophagia and gliosis, and Gallyas-Braak silver staining revealed argyrophilic threads and granular or fibrous inclusion bodies. These findings were consistent with CBD as a cause of the atrophy. The degeneration of motor nerve nuclei, including the oculomotor and abducens nuclei, in the brain stem tegmentum was also noted, but no corresponding imaging findings were seen in the present study.

The localization of SCWM abnormalities, though different from those in previous reports,[1,15] was prominent in the present study. In CBD, Tokumaru et al,[15] Doi et al,[16] and Koyama et al[1] described predominantly unilateral SCWM abnormalities on T2-weighted imaging and FLAIR. In their re-

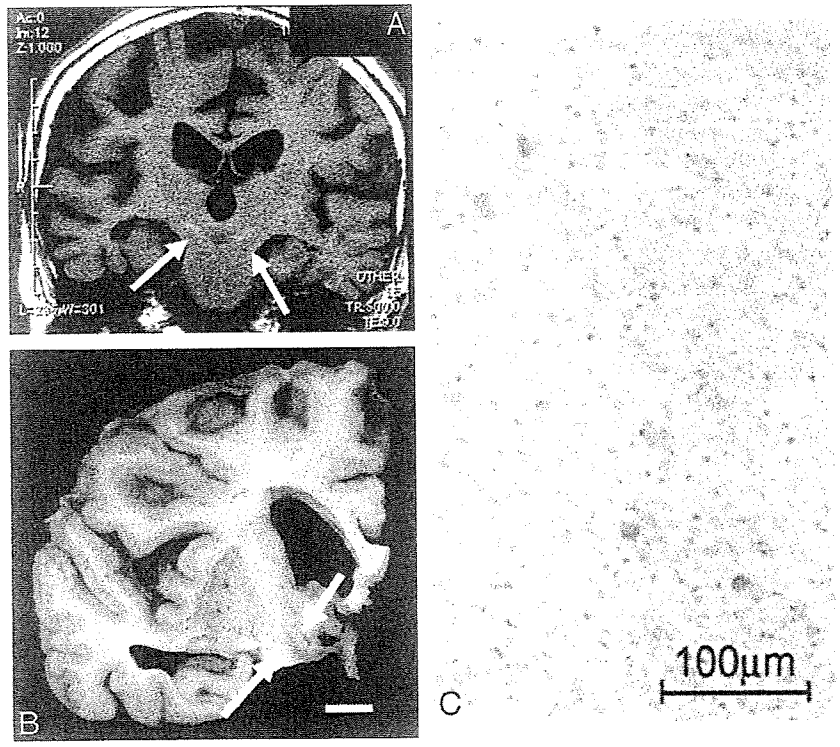

Fig 9. Corticobasal degeneration (CBD), case 1. An 84-year-old woman. *A,* Coronal T1-weighted image shows symmetric high signal intensity bilaterally in the subthalamic nuclei (*arrows*). *B,* A macroscopic specimen shows a brownish change in the subthalamic nuclei (*arrows*). *C,* On microscopic examination (AT8 stain), antiphosphorylated tau antibody–positive neurons and gliosis are observed. These changes are characteristic of CBD. The scale is 100 μm.

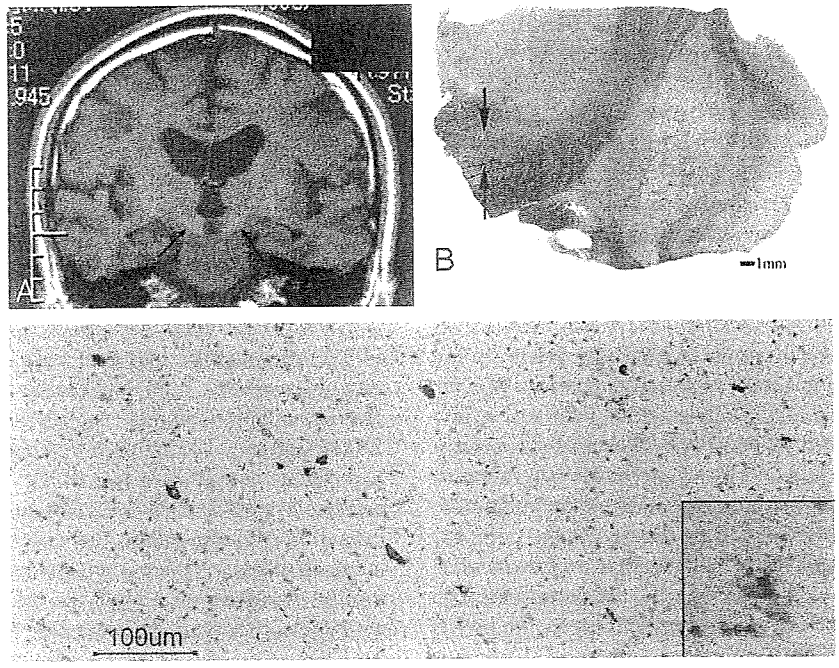

Fig 10. Progressive supranuclear palsy (PSP). An 84-year-old man. *A,* Coronal T1-weighted image shows a symmetric high signal intensity bilaterally in the subthalamic nuclei (*arrow*). *B,* A microscopic specimen of myelin-sheath staining shows the atrophic change of the subthalamic nuclei (*arrows*). The scale is 1 mm. *C,* On microscopic examination in the subthalamic nuclei, AT8 staining is clearly positive in the neurons (brown area). An enlarged image shows a tuft. These changes are characteristic of PSP. The scale is 100 μm.

ports, localization in the precentral gyrus of the SCWM and signal-intensity abnormalities contralateral to the clinically affected side were noted.[1,15] However, in the present study, the localization of white matter signal-intensity abnormalities differed among the 3 cases. In particular, in case 3, T2-weighted imaging and FLAIR showed widespread signal-intensity changes in the frontal lobe white matter bilaterally. This appearance differed from that reported by Doi et al[16] and Koyama et al.[1] In 2 patients, signal-intensity abnormalities were present in the superior frontal gyrus white matter. Only 1

patient showed signal-intensity abnormalities in the precentral gyrus SCWM. It is important to recognize the possibility of CBD showing different localizations of atrophy and white matter signal-intensity abnormalities rather than findings in the more typical cases as reported by Koyama et al.[1] In cases without predominantly unilateral cortical signs on clinical evaluation, the localization of atrophy and SCWM signal-intensity abnormalities may differ from typical cases. In these cases, MR imaging findings of high signal intensity in the subthalamic nucleus on T1-weighted images and severe atrophy of the midbrain tegmentum on midsagittal sections can provide useful information.

Rebeiz et al[17] first reported CBD with distinct features and a clinically asymmetric onset characterized by apraxia, dystonia, postural instability, and an akinetic-rigid syndrome that does not respond to levodopa, but since then, cases presenting with dementia, in which Alzheimer or Pick disease must be ruled out, and cases with other clinical features, in which PSP must be ruled out, have been reported.[18-21] A variety of underlying neuropathologic features have also been reported. Recent reports clarified the presence of many phenotypes of CBD neuropathologically and clinically.[10-14] Although there were only 4 cases, it was difficult to diagnose CBD clinically in cases definitely diagnosed neuropathologically, and 1 case showed imaging findings different from those previously reported. The lesions in the white matter widely expanded bilaterally in case 3, indicating that the clinical features alone did not confirm CBD. This case probably represents a new clinical phenotype of CBD.

Neuropathologic examination of SCWM lesions that correlated with the MR imaging findings showed the typical tauopathy of CBD. The degenerative changes were characteristic of CBD. In 1996, we suggested, on the basis of the neuropathologic findings in CBD, that white matter lesions of the frontal lobe were secondary degenerative changes.[15] Doi et al[16] and Koyama et al[1] also believe that these white matter lesions in CBD reflect the progression of neuronal degeneration, especially demyelination secondary to axonal loss or change. However, in the present study, at sites where MR imaging showed white matter lesions, though neuropathologic examination revealed some secondary degeneration, tauopathy in the white matter, particularly the SCWM, was clearly evident. This shows a positive radio-pathologic correlation of these changes in CBD. In 2002, Dickson et al[8] proposed neuropathologic criteria, with a primary emphasis on tau-positive neuronal and glial lesions, for the diagnosis of CBD. Advances in neuropathologic staining methods to evaluate tau have expanded our knowledge of these primary changes in CBD. Dickson et al also confirmed tauopathy of the white matter in CBD. After the report of Dickson et al, the neuropathologic evaluation criteria for lesions in the white matter apparently changed, and the finding that lesions in the white matter were primary degeneration in CBD, not secondary, may be important new information for the evaluation of an association with clinical and pathologic findings. In the present cases, degeneration was severe, affecting U-fibers, which should be investigated to collate with MR images.

T1-weighted images, obtained in 3 patients with CBD, showed symmetric high-intensity signals in the subthalamic nucleus. This finding was also present in a high proportion of patients with PSP, making an MR imaging–based differential diagnosis difficult. Neuropathology of sites corresponding to these signal-intensity changes showed tauopathy-related degeneration. Gliosis was also present, but on T2-weighted imaging and FLAIR, signal-intensity changes were difficult to detect. Only axial sections were obtained on T2-weighted imaging. These may have been insufficient to delineate the subthalamic nucleus adequately. In PSP, there was a high rate of similar findings, so these were not useful in the differential diagnosis. In all patients with PSP, the neuropathology showed more severe degeneration than in those with CBD. In addition to midbrain tegmentum atrophy, the localization of degeneration was similar in CBD to that seen in PSP. These signal-intensity changes were only visually evaluated by the neuroradiologists in the limited number of cases, but no signal-intensity change was noted in the pathologically healthy group, suggesting that primary degenerative findings of the individual diseases in the subthalamic nuclei and abnormal signals in this region are significant to some extent. However, differentiating CBD and PSP based on these findings alone is not possible. Therefore, a combination of imaging findings, including the presence of white matter signal-intensity changes and asymmetric atrophy, is important in correctly diagnosing CBD.

Conclusions

The correlation between radiologic and pathologic findings was investigated in patients with CBD, and MR imaging findings that could be used to differentiate CBD from PSP clinically were identified.

In CBD, midbrain tegmentum atrophy was severe, and degeneration in this area was correlated with the severity. However, this finding did not help in the differential diagnosis distinguishing CBD from PSP. T1-weighted imaging showed symmetric high-intensity signals in the subthalamic nucleus, but a large proportion of patients with PSP had a similar finding. On neuropathologic examination, each disorder showed characteristic degeneration. The degree of degeneration was more severe in PSP, but no imaging-based differences were observed. In CBD, there was a high rate of atrophy contralateral to the clinically affected side, with extension to the central sulcus. This suggests that the localization of atrophy differs depending on the underlying etiology. In PSP, unilateral atrophy was not a predominant finding.

MR imaging, FLAIR, and T2-weighted imaging showed high signal intensities in the SCWM. Previous studies have correlated this finding with secondary degeneration. The present study is the first to correlate these SCWM signal-intensity changes with primary degeneration in CBD. In addition, the localization of white matter lesions was correlated with a variety of clinical phenotypes. This suggests that there are CBD types other than those that are localized only to the precentral gyrus SCWM.

References

1. Koyama M, Yagishita A, Nakata Y, et al. **Imaging of corticobasal degeneration syndrome.** *Neuroradiology* 2007;49:905–12
2. Oba H, Yagishita A, Terada H, et al. **New and reliable MRI diagnosis for progressive supranuclear palsy.** *Neurology* 2005;28:2050–55
3. Saito Y, Murayama S. **Neuropathology of mild cognitive impairment.** *Neuropathology* 2007;27:578–84
4. Mirra SS, Heyman A, McKeel D, et al. **The Consortium to Establish a Registry**

for Alzheimer's Disease (CERAD). Part II. Standardization of the neuropathologic assessment of Alzheimer's disease. *Neurology* 1991;41:479–86
5. Saito Y, Ruberu NN, Sawabe M, et al. **Lewy body-related alpha-synucleinopathy in aging.** *J Neuropathol Exp Neurol* 2004;63:742–49
6. McKeith IG, Galasko D, Kosaka K, et al. **Consensus guidelines for the clinical and pathologic diagnosis of dementia with Lewy bodies (DLB): report of the consortium on DLB international workshop.** *Neurology* 1996;47:1113–24
7. Braak H, Braak E. **Neuropathological stageing of Alzheimer-related changes.** *Acta Neuropathol* 1991;82:239–59
8. Dickson DW, Bergeron C, Chin SS, et al. **Office of Rare Diseases Neuropathologic Criteria for corticobasal degeneration.** *J Neuropathol Exp Neurol* 2002;61:935–46
9. Hauw JJ, Daniel SE, Dickson D, et al. **Preliminary NINDS neuropathologic criteria for Steele-Richardson-Olszewski syndrome (progressive supranuclear palsy).** *Neurology* 1994;44:2015–19
10. Mathuranath PS, Xuereb JH, Bak T, et al. **Corticobasal ganglionic degeneration and/or frontotemporal dementia? A report of two overlap cases and review of literature.** *J Neurol Neurosurg Psychiatry* 2000;68:304–12
11. Grimes DA, Lang AE, Bergeron CB. **Dementia as the most common presentation of cortical-basal ganglionic degeneration.** *Neurology* 1999;53:1969–74
12. Schneider JA, Watts RL, Gearing M, et al. **Corticobasal degeneration: neuropathologic and clinical heterogeneity.** *Neurology* 1997;48:959:969
13. Rinne JO, Lee MS, Thompson PD, et al. **Corticobasal degeneration: a clinical study of 36 cases.** *Brain* 1994;117:1183–96
14. Bergeron C, Pollanen MS, Weyer L, et al. **Unusual clinical presentations of cortical-basal ganglionic degeneration.** *Ann Neurol* 1996;40:893–900
15. Tokumaru AM, O'uchi T, Kuru Y, et al. **Corticobasal degeneration: MR with histopathologic comparison.** *AJNR Am J Neuroradiol* 1996;17:1849–52
16. Doi T, Iwasa K, Makifuchi T, et al. **White matter hyperintensities on MRI in a patient with corticobasal degeneration.** *Acta Neurol Scand* 1999;99:199–201
17. Rebeiz JJ, Kolodny EH, Richardson EP Jr. **Corticodentatonigral degeneration with neuronal achromasia: a progressive disorder of late adult life.** *Trans Am Neurol Assoc* 1967;92:23–26
18. Brown J, Lantos PL, Roques P, et al. **Familial dementia with swollen achromatic neuron and corticobasal inclusion bodies: a clinical and pathological study.** *J Neurol Sci* 1996;135:21–30
19. Doran M, du Plessis DG, Enevoldson TP, et al. **Pathological heterogeneity of clinically diagnosed corticobasal degeneration.** *J Neurol Sci* 2003;216:127–34
20. Feany MB, Mattiace LA, Dickson DW. **Neuropathologic overlap of progressive supranuclear palsy, Pick's disease, and corticobasal degeneration.** *J Neuropathol Exp Neurol* 1996;55:53–67
21. Jendroska K, Rossor MN, Mathias CJ, et al. **Morphological overlap between corticobasal degeneration and Pick's disease: a clinicopathological report.** *Mov Disord* 1995;10:111–14

Please cite this article in press as: Sato et al., Spinocerebellar Ataxia Type 31 Is Associated with "Inserted" Penta-Nucleotide Repeats Containing $(TGGAA)_n$..., The American Journal of Human Genetics (2009), doi:10.1016/j.ajhg.2009.09.019

ARTICLE

Spinocerebellar Ataxia Type 31 Is Associated with "Inserted" Penta-Nucleotide Repeats Containing $(TGGAA)_n$

Nozomu Sato,[1,13] Takeshi Amino,[1,2,3,13] Kazuhiro Kobayashi,[4] Shuichi Asakawa,[5] Taro Ishiguro,[1] Taiji Tsunemi,[1] Makoto Takahashi,[1] Tohru Matsuura,[6] Kevin M. Flanigan,[7] Sawa Iwasaki,[8] Fumitoshi Ishino,[8] Yuko Saito,[9] Shigeo Murayama,[9] Mari Yoshida,[10] Yoshio Hashizume,[10] Yuji Takahashi,[11] Shoji Tsuji,[11] Nobuyoshi Shimizu,[12] Tatsushi Toda,[4] Kinya Ishikawa,[1,*] and Hidehiro Mizusawa[1,2]

Spinocerebellar ataxia type 31 (SCA31) is an adult-onset autosomal-dominant neurodegenerative disorder showing progressive cerebellar ataxia mainly affecting Purkinje cells. The SCA31 critical region was tracked down to a 900 kb interval in chromosome 16q22.1, where the disease shows a strong founder effect. By performing comprehensive Southern blot analysis and BAC- and fosmid-based sequencing, we isolated two genetic changes segregating with SCA31. One was a single-nucleotide change in an intron of the thymidine kinase 2 gene (*TK2*). However, this did not appear to affect splicing or expression patterns. The other was an insertion, from 2.5–3.8 kb long, consisting of complex penta-nucleotide repeats including a long $(TGGAA)_n$ stretch. In controls, shorter (1.5–2.0 kb) insertions lacking $(TGGAA)_n$ were found only rarely. The SCA31 repeat insertion's length inversely correlated with patient age of onset, and an expansion was documented in a single family showing anticipation. The repeat insertion was located in introns of *TK2* and *BEAN* (brain expressed, associated with Nedd4) expressed in the brain and formed RNA foci in the nuclei of patients' Purkinje cells. An electrophoretic mobility-shift assay showed that essential splicing factors, serine/arginine-rich splicing factors SFRS1 and SFRS9, bind to $(UGGAA)_n$ in vitro. Because $(TGGAA)_n$ is a characteristic sequence of paracentromeric heterochromatin, we speculate that the insertion might have originated from heterochromatin. SCA31 is important because it exemplifies human diseases associated with "inserted" microsatellite repeats that can expand through transmission. Our finding suggests that the ectopic microsatellite repeat, when transcribed, might cause a disease involving the essential splicing factors.

Introduction

Autosomal-dominant cerebellar degenerative disorders are generally referred to as spinocerebellar ataxia (SCA).[1] Clinically, progressive cerebellar ataxia is the cardinal neurological symptom, and it is often accompanied by variable extracerebellar neurological features, such as pyramidal tract signs, extrapyramidal signs, ophthalmoparesis, and sensory disturbances. Neuropathologically, the cerebellum and its related systems, such as the brainstem, spinal cord, and basal ganglia, can be involved to various degrees.

Nearly 30 genetic loci have been identified. Of these, expansions of tri-nucleotide (CAG) repeats are the causes of SCA1 (MIM #164400); SCA2 (MIM #183090); SCA3, or Machado-Joseph disease (MJD) (MIM #109150); SCA6 (MIM #183086), SCA7 (MIM #164500); SCA17 (MIM #607136); and dentatorubral-pallidoluysian atrophy (DRPLA) (MIM #125370). These disorders, together with Huntington disease (HD) (MIM +143100) and spinal and bulbar muscular atrophy (MIM #313200), are called polyglutamine diseases[2] because the CAG repeats, which are expanded in patients, reside in the coding regions and are translated into polyglutamine tracts. SCA8 (MIM #608768), SCA10 (MIM #603516), and SCA12 (MIM #604326) are caused by expansions of both CTG and CAG; ATTCT; and CAG repeats, respectively, in the non-coding regions of the responsible genes. These disorders, together with myotonic dystrophy type 1 (DM1) (MIM #160900), DM2 (MIM #602668), HD-like disease type 2 (HDL2) (MIM #606438), and Fragile X tremor/ataxia syndrome (FXTAS) (MIM #300623), caused by RNA-mediated gain-of-function mechanisms, are called noncoding repeat expansion disorders[3]. These are dynamic repeat-expansion disorders, but some forms of SCA are caused

[1]Department of Neurology and Neurological Science, Graduate School, Tokyo Medical and Dental University, Yushima 1-5-45, Bunkyo-ku, Tokyo 113-8519, Japan; [2]The 21st Century Center of Excellence Program, Brain Integration and Its Disorders, from the Ministry of Education, Science and Culture, Tokyo 113-8519, Japan; [3]Tokyo Medical and Dental University Hospital, Faculty of Medicine, Yushima 1-5-45, Bunkyo-ku, Tokyo 113-8519, Japan; [4]Division of Clinical Genetics, Department of Medical Genetics, Osaka University Graduate School of Medicine, Yamada-oka 2-2, Suita, Osaka 565-0871, Japan; [5]Department of Molecular Biology, Keio University School of Medicine, Shinanomachi 35, Shinjuku-ku, Tokyo 160-8582, Japan; [6]Division of Neurogenetics and Bioinformatics, Center for Neurological Diseases and Cancer, Nagoya University Graduate School of Medicine, Tsurumai-cho 65, Showa-ku, Nagoya 466-8550, Japan; [7]Department of Neurology and Eccles Institute of Human Genetics, University of Utah, 15 North 2030 East Rm. 4420, Salt Lake City, UT 84132, USA; [8]Department of Epigenetics, Medical Research Institute, Tokyo Medical and Dental University, Yushima 1-5-45, Bunkyo-ku, Tokyo 113-8519, Japan; [9]Department of Geriatric Neuroscience, Tokyo Metropolitan Institute of Gerontology, Sakaecho 35-2, Itabashi-ku, Tokyo 173-0015, Japan; [10]Department of Neuropathology, Institute for Medical Science of Aging, Aichi Medical University, Nagakute-cho, Aichi-gun, Aichi 480-1195, Japan; [11]Department of Neurology, University of Tokyo Graduate School of Medicine, Hongo 7-3-1, Bunkyo-ku, Tokyo 113-8655, Japan; [12]Advanced Research Center for Genome Super Power, Keio University, Okubo 2, Tsukuba, Ibaraki 300-2611, Japan
[13]These authors contributed equally to this work
*Correspondence: pico.nuro@tmd.ac.jp
DOI 10.1016/j.ajhg.2009.09.019. ©2009 by The American Society of Human Genetics. All rights reserved.

by static mutations (e.g., missense, frameshift, or deletion) in functionally important genes,[4] such as β-III spectrin (*SPTBN2*) (MIM #604985) in SCA5 (MIM #600224), tau tubulin kinase 2 (*TTBK2*) (MIM #611695) in SCA11 (MIM #604432), voltage-gated potassium channel (*KCNC3*) (MIM #176264) in SCA13 (MIM #605259), protein kinase C γ (*PRKCG*) (MIM #176980) for SCA14 (MIM #605361), inositol 1,4,5-triphosphate receptor type 1 (*ITPR1*) (MIM #147265) in SCA15 (MIM #606658), and fibroblast growth factor 14 (*FGF14*) (MIM #601515) in SCA27 (MIM #609307). The fact that so many mutations result in the SCA phenotype in humans suggests that the cerebellum and its related nervous systems have particularly sophisticated and vulnerable neurobiological characteristics.

We previously mapped a form of SCA (previously called "chromosome 16q22.1-linked autosomal dominant cerebellar ataxia [ADCA]"; MIM #117210 and newly termed as "SCA31"in this report) to human chromosome 16q22.1.[5,6] This locus was already known for a clinically distinct ataxia, SCA4[7] (MIM %600223). SCA31 presents as pure cerebellar ataxia with an average age of onset of 61.2 years and thus is the latest to appear of all SCAs.[6,8] The Purkinje cell, the only projecting neuron in the cerebellar cortex, is predominantly affected.[8] SCA31 is estimated to rank as the third most frequent SCA in Japan, after SCA3 (MJD) and SCA6. In SCA4, in contrast, cerebellar ataxia is always accompanied by both sensory axonal neuropathy and reduced or absent tendon reflexes, and Babinski's signs may be also seen.[7,9] The age of onset is usually in the third or fourth decade, and neuropathologically, the degeneration of multiple systems is observed.[10] Only two families have been genetically confirmed as having SCA4: one is the original SCA4 family that is of Scandinavian origin but resides in the United States,[7] and the other is a German family.[9] Discovery of the mutations is needed to settle the question as to whether SCA4 and SCA31 are allelic diseases.[11]

We previously reported that a single-nucleotide change (−16C > T) in the *PLEKHG4* (*puratrophin-1*) gene (MIM *609526) is tightly associated with SCA31.[6] However, two patients who did not have this change were subsequently found[12,13], indicating that the −16C > T change in *PLEKHG4* is a marker in a strong linkage disequilibrium with SCA31 but is not the cause of this disease. Conducting fine SNP typing allowed the SCA31 critical region to be tracked to a 900 kb "founder" chromosome lying between rs11640843 (SNP04[13]) and −16C > T in *PLEKHG4*.[6] Whereas all SCA31 patients shared a single haplotype for this critical region, none of the controls (800 Japanese and 60 white American control chromosomes) had it, indicating that SCA31 is caused by a single founder mutation.[13] Previous attempts to find this mutation by PCR-based sequencing in all annotated coding exons and expressed sequence tags (ESTs) failed. The strong founder effect in SCA31 made a mutation search complicated because segregating genetic changes are not always causative. Therefore, we needed to identify all the genetic changes and then investigate which one was the causative mutation.

In this study, we carried out a comprehensive mutation search, including Southern blot analysis to detect any chromosomal rearrangements and BAC- and fosmid-based complete genome sequencing to identify all the genomic changes in the 900 kb critical region. Here we show that SCA31 is associated with an inserted sequence that consists of complex penta-nucleotide repeats containing $(TGGAA)_n$.

Material and Methods

Human Samples

Study Subjects

We collected blood samples after obtaining informed consent from all involved SCA31 families, a small nuclear family of American SCA4 kindred[7], and controls. The study conformed to the tenets of the Declaration of Helsinki, and the ethics were approved by the institutional review board of Tokyo Medical and Dental University, Tokyo, Japan.

Genomic DNA was extracted on the basis of a standard protocol.[6] The SCA31 subjects studied were 160 affected individuals from 98 SCA31 families, consisting of the previously described 125 affected individuals from 64 families[13], an individual from the "U09" family without the −16C > T *PLEKHG4* change[13], and 34 newly recruited individuals from 33 families. Normal controls consisted of 400 Japanese and 30 white American individuals, in whom no personal or family histories of ataxia or any inherited disorders had been documented. Five individuals from the original SCA4 kindred (kindred 1875[7]), including three with typical SCA4 symptoms and SCA4 disease-haplotypes, were also studied. In addition, the previously described 21 individuals[13] who had a similar clinical phenotype but did not carry the SCA31 founder haplotype were also included as disease controls for mutation analysis.

Among the SCA31 individuals, one homozygous patient in family P2[14] who harbored two identical SCA31 haplotypes between D16S3094 and D16S3095, covering the SCA31 critical interval, was chosen for a complete BAC- and fosmid-based genomic sequencing of the SCA31 critical region. The same homozygous patient, a heterozygous SCA31 patient in family P14[5], and a normal control (control 1) were chosen for investigation by Southern blotting, quantitative genomic PCR, and array-based comparative genomic hybridization (aCGH) analyses. Mutation candidates found through these analyses were then screened in the remaining SCA31 and control individuals.

The penta-nucleotide repeat insertion (see Results) was tested either by Southern blotting, PCR, or both in all SCA31 individuals, five individuals from an SCA4 family, and all controls (430 normal controls and 21 disease controls). Thirty-nine SCA31 heterozygous patients, from whom we could obtain detailed clinical information and ages of onset, were analyzed for the correlation between insert length and age of onset. One affected SCA4 individual and ten disease controls were screened for mutations in the critical genes, *BEAN* (brain expressed, associated with Nedd4) (MIM *612051) and *TK2* (thymidine kinase 2) (MIM *188250), and in EST *FLJ27243* (see Results) by PCR and direct sequencing.

Brain Tissue Samples

Frozen brain tissues of the cerebellar cortex were used for gene expression analyses (i.e., RT-PCR, TaqMan quantitative RT-PCR

analyses, and fluorescence in situ hybridization [FISH]). In addition to the cerebellar cortex, the cerebral white matter (frontal lobe), the frontal cortex, hippocampus, thalamus, and the midbrain from a control individual were studied for RT-PCR analysis. Both control and SCA31 brains were obtained during an autopsy performed under their families' written consent and approved by each institutional ethics committee. These brains were immediately frozen and stored at −80°C until use. Four control frozen brains were studied: two were from patients with sporadic amyotrophic lateral sclerosis (ages at death: 70 and 78 years), one was from a patient with SCA3/MJD (age at death: 65 years), and one was from a patient who had autosomal-dominant progressive external ophthalmoplegia (adPEO) (MIM #157640) and a heterozygous missense mutation in the nuclear-encoded DNA polymerase-γ gene (age at death: 72 years). Neuropathological examinations of these patients did not show obvious neuronal losses in the cerebella. For SCA31, two patients were studied (ages at death: 74 and 78 years).

Mutation screening

Southern Blotting

We screened for genomic rearrangement by performing Southern blot analysis and using cosmid clones for probe synthesis. The method has been previously described.[6,15] In brief, we generated cosmid clones, tandemly covering the SCA31 critical region, by subcloning from the BAC contig constructed on the basis of a control human genome.[16] Probes radiolabeled with ^{32}P were then generated from each cosmid clone. Genomic DNA extracted from lymphoblastoid cell lines of three individuals (one control individual, an SCA31 homozygote, and a heterozygote) was digested with a restriction enzyme and subjected to Southern blot analysis. The analysis was undertaken with five different restriction enzymes (BamHI, EcoRI, EcoRV, HindIII and XbaI). When needed to confirm results, another five SCA31 subjects and ten normal controls were similarly investigated.

Altered restriction enzyme fragment patterns were observed with the cosmid probe detecting the genomic region between 65,083,571 and 65,124,051 on NCBI Build 36.3. We confirmed the results by employing PCR products as a probe that had been obtained by amplification of a 3009 bp segment (from 65,079,127–65,082,135) within this genomic region and radiolabeled with ^{32}P. This PCR reaction was carried out with primers Ins-long3.0k-F (5′-GCTTCTCTGCTTCTGTCATCAGCTCAC-3′) and Ins-long3.0k-R (5′-ATCTTTCCACACTACCATCCCATCCAG-3′); control genomic DNA was used as a template.

Sequencing of the 900 kb SCA31 Critical Region

This was performed by a modified version of the methods used in Chromosome 21 genome sequencing.[17,18]

Construction of a BAC Library of the Genomic DNA from the Lymphoblastoid Cell Line Derived from a Homozygous SCA31 Patient. The lymphoblastoid cells derived from the homozygous SCA31 patient[14] were embedded in agarose gel plugs, and high-molecular-weight genomic DNA was extracted. The DNA was partially digested with HindIII, and fragments from 100–150 kb were selected by pulse field gel electrophoresis (PFGE). The collected DNA fragments were ligated with pBAC-lac[18] and subsequently used for transformation of DH10B cells by electroporation.

Transformed *E. coli* were spread on lysogeny broth (LB) plates with 12.5×10^{-3} g/liter of chloramphenicol, X-gal (5-bromo-4-chloro-3-indolyl-b-D-galactopyranoside), and IPTG (isopropyl β-D-1-thiogalactopyranoside). Positive colonies were selected by color, picked up, and separately stored in LB liquid medium with 7.5% (v/v) glycerol and 12.5×10^{-3} g/liter chloramphenicol (LB-glycerol-Cm) prepared in 384-well plates. A total of approximately 115,000 clones were obtained. In order to evaluate the quality of the BAC library, we randomly selected 200 clones, isolated their BAC DNA by the alkaline-SDS (sodium dodecyl sulfate) method, and digested it with NotI. Their insert sizes were measured by PFGE. Approximately 90% of BAC clones had DNA inserts of 80–140 kb in length, and the mean size was approximately 110 kb.

Construction of a Fosmid Library of the Genomic DNA of the Same Homozygous Patient. Genomic DNA extracted from the lymphoblastoid cell line from the same homozygous patient[14] was sheared, and fragments ranging in length from 35–50 kb were collected. The DNA fragments were cloned into pCC1FOS vector (Epicenter) with the CopyControl Fosmid Library Production Kit (Epicenter) according to the manufacturer's instructions. Approximately 250,000 clones were collected in LB-glycerol-Cm pools, each of which contained 2,000–10,000 clones. Examination of 96 randomly selected clones confirmed that each clone harbored a DNA insertion of approximately 35–45 kb.

Identification of BAC and Fosmid Clones Covering the SCA31 Critical Region. We spotted approximately 115,000 BAC clones in a grid pattern on GeneScreen Plus membranes (PerkinElmer) with a 4 × 4 double offset pattern by using a BioGrid robot (BioRobotics) to make high-density replica (HDR) filters. We created probes by amplifying the genomic DNA of the same patient by PCR to detect every 50 kb segment in the critical region. After labeling the probes with ^{32}P, we hybridized the HDR filters with them. Fifty-two BAC clones were identified as positive clones. The insert ends of these 52 BAC clones were sequenced, and 48 clones were mapped to the 900 kb critical region, whereas the remaining fell into different chromosomal regions.

We constructed a fosmid library to clone the genomic region (approximately 42.3 kb in length) that was missed in the BAC library. Four sites in the region were chosen as PCR targets, and primers that would allow their specific amplification were used. By serial PCR, the pools identified as harboring the desired clones were divided into smaller pools, and subsequently three fosmid clones covering the 42.3 kb region were isolated.

Complete Sequencing of the BAC and Fosmid Clones Covering the 900 kb Critical Region. Twelve BAC and three fosmid clones formed a contig that covered the entire 900 kb critical region and thus were rendered for sequencing (Table 1). The complete base sequences of all but one BAC clone (Ca0215J24) and one fosmid clone (CaFos003) were determined by shotgun sequencing as previously described.[17] In brief, every BAC and fosmid clone was sheared into short fragments of approximately 4 kb, treated with shrimp alkaline phosphatase, and then subcloned into pCR-blunt II vector (Invitrogen). The plasmid was used for transforming DH10B by electroporation. Seven hundred and sixty-eight subclones from each BAC clone and 384 subclones from each fosmid clone were picked up. Each was inoculated into 160 μl of LB with glycerol and kanamycin, grown overnight, and then rendered for rolling-circle amplification (RCA) with the Templiphi DNA Amplification Kit (GE Healthcare Bioscience). Amplified subclone plasmids were sequenced with M13 primers and the BigDye Terminator v3.1 Cycle Sequencing Kit (Applied Biosystems) in ABI PRISM 3730 and 3100 (Applied Biosystems). The raw sequence data were analyzed and assembled with phred, phrap, and consed. The remaining two clones, Ca0215J24 and CaFos003, were sequenced so that the gaps between Ca0217F15 and Ca0262A14 and between CaFos001 and CaFos002, respectively, could be filled.

Table 1. Genomic Regions Cloned by 12 BACs and Three Fosmids that Were Rendered for Sequencing

	Cloned region on NCBI Build 36.3	
BAC or Fosmid Clone	**from**	**to**
Ca0109N14	64,935,119	65,053,675
Ca0159N04	65,052,547	65,166,347
Ca0041G15	65,163,955	65,252,631
Ca0080M24	65,215,426	65,328,653
Ca0303C23	65,265,426	65,358,989
CaFos001	65,345,373	65,382,103
CaFos003	65,369,225	65,410,300
CaFos002	65,385,244	65,430,086
Ca0151F23	65,401,149	65,500,053
Ca0312C05	65,485,609	65,608,342
Ca0238A16	65,530,876	65,635,257
Ca0217F15	65,634,014	65,724,706
Ca0215J24	65,692,848	65,788,160
Ca0262A14	65,726,364	65,829,738
Ca0154D03	65,815,462	65,917,148

Together, the 12 BACs and three fosmids formed a contig covering the entire 900 kb critical region.

Finally, the obtained nucleotide sequence information in the SCA31 critical interval of the homozygous patient was compared with a public database (NCBI, build 36.3). For each discordant nucleotide sequence, 20 pilot control individuals were examined so that it could be determined whether such discordance was simply due to polymorphism. If the discordance was not proven to be polymorphism, a larger number of controls (n = 430) and SCA31 patients were analyzed. With this approach, nucleotide sequences that segregate with SCA31 in the entire 900 kb critical region were searched.

Quantitative Genomic PCR and aCGH

Quantitative genomic PCR was performed with TaqMan probes (Applied Biosystems) designed to measure two exons of each gene within the SCA31 critical region as previously described.[19] Gene dosage was also analyzed by custom-designed, high-definition array-based comparative genomic hybridization (aCGH) microarrays (Agilent Technologies). Oligonucleotide probes were designed by two of us (Y.T. and S.T.) according to the published method.[20,21] A 1.88 Mb genomic region between D16S3031 and D16S3107 (NCBI, build 36.3), completely covering the 900 kb SCA31 critical region, was included in the microarray, and probes were designed with an average interval of 100 bp. Genomic DNA samples of three individuals (one homozygous patient,[14] one heterozygous patient, and one control subject) were tested and compared with each other.

Characterizing the Penta-Nucleotide Repeat Insertion

Analysis of the Penta-Nucleotide Repeat Length by PCR and Agarose-Gel Electrophoresis

The genomic DNA of the patients was amplified by PCR with primers 1.5k-ins-F (5′- ACTCCAACTGGGATGCAGTTTCTCAAT-3′) and 1.5k-ins-R (5′- TGGAGGAAGGAAATCAGGTCCCTAAAG-3′). Each PCR reaction was performed in a final volume of 10 μl, containing 0.25 μM of each primer, 400 μM (each) of dNTP, 1.5 mM of MgCl2, 0.25 U of LA Taq HS polymerase (Takara Bio), and 50–100 ng of genomic DNA. Thermal cycles were as follows: initial denaturing at 95°C for 5 min followed by 30 cycles of denaturing at 95°C for 20 s and annealing and extension at 68°C for 8 min. Five microliters (5 μl) of each PCR product was digested with HaeIII and then run through an 0.8% agarose gel at 30 V (V) for 15 hr with 1 kb DNA Ladder (Takara Bio). When multiple members were collected, differences in the length of insertion were analyzed in the same gel.

The lengths (L = length) of HaeIII-digested PCR products (L/kb) were calculated as below. The electrophoretic migration distance (d; in millimeters) of each sample was measured and then introduced into the formula: $d = a\ln L + b$, in which "a" and "b" were determined by the standard line obtained from the data of the size markers. As the HaeIII-digested PCR product has 193-bp sequences flanking the SCA31 penta-nucleotide repeat insertion, the length of the insertion was calculated as L − 0.19/kb. The correlation between the length of the repeat insertion and the age of onset was analyzed via calculation of Pearson's product-moment correlation coefficient (r).

Sequencing of the Penta-Nucleotide Repeat in SCA31 Patients and Two Controls

PCR products including the penta-nucleotide repeat were obtained as described in the previous section. We first analyzed the repeat sequences in five SCA31 patients by direct sequencing of the gel-extracted, purified PCR product with primers 010-1F (5′-CATAGTGGCACATGCATGTAGTC-3′) and 10R (5′-CCCAGGC TGGAGTGCAGTGAC-3′) to see the configurations of the insertion sequences. Using the same method, we investigated nucleotide sequences at the insertion site in five normal controls so that we could see the $(TAAAA)_n$ repeat numbers (see Results). Because we found two exceptional controls (controls 1 and 2) harboring smaller insertions, we also sequenced these insertions by the same method.

Because the simple repeat sequences in the insertion extended too long to be read through, shotgun sequencing was also performed in the homozygous patient and on the allele with an insertion from control 1. For this shotgun sequencing, purified PCR products were directly sheared by HydroShear (Genomic Solutions). Ninty-six colonies were picked up for each PCR product and sequenced as n BAC and fosmid shotgun sequencing. The obtained sequence data were assembled and analyzed with phred, phrap, and consed.

Analysis of Gene Expression

Poly-A^+ RNA obtained from frozen human cerebellar tissues was reverse-transcribed with SuperScript III (Invitrogen). Because the insertion site was not annotated in the public database as being associated with any genes, we independently examined whether the repeat insertion could be transcribed. We designed primers around the repeat insertion site with 300–1000 bp intervals and attempted to amplify the site by PCR with various pairings of primers. If amplification was successful, we cloned the PCR products into pCR2.1-TOPO (Invitrogen) and cycle-sequenced them to find previously unidentified transcripts.

Gene expression in various human tissues was examined by PCR with the primers listed in Table S1. Human Multiple Tissue Panels I and II (Clontech, BD Bioscience) as well as various brain regions obtained from control brains at autopsy were used. For the identification of full-length transcripts, 5′- and 3′-rapid cloning of the

cDNA ends (RACE) and RT-PCR analysis of control human cerebellar cDNA were performed. Expressions of newly identified transcripts were also confirmed by PCR screening of a human cerebellar cDNA library (Takara Bio, Inc.). When necessary, strand-specific RT-PCR was performed according to the method previously described.[22]

Quantitative RT-PCR

Quantitative PCR of cDNA was carried out by the TaqMan expression chemistry protocol with an ABI Prism 7700 Sequence Detection System (Applied Biosystems). Primers and probes used in this study were designed by the manufacturer (Table S2). Quantities measured by analysis were adjusted for glyceraldehyde 3-phosphate dehydrogenase (GAPDH) with TaqMan GAPDH Control Reagents (Applied Biosystems). Analyses were repeated three times for each sample, and results were compared between the patient (n = 2) and control (n = 4) groups.

Fluorescence In Situ Hybridization for Detecting RNA Foci

The detection of the repeat transcripts in Purkinje cells by FISH was carried out as previously described[23] with digoxigenin (DIG)-labeled, locked nucleic acid (LNA) probes (Exiqon) (Table S3). The brain samples of the two SCA31 patients and four control subjects were analyzed in this part of the study. Frozen cerebellar cortex samples obtained at autopsy were stored at −80°C and sectioned at 10 μm thickness in a cryostat. Sections were fixed for 30 min at room temperature in 4% paraformaldehyde in PBS. After fixation, sections were washed and treated with 50% formamide, 2× SSC (300 mM NaCl and 30 mM sodium citrate [pH 7.0]) for 10 min at room temperature. Sections were then hybridized overnight at 37°C with a solution containing probe (1 ng/μl), 40% formamide, 2× SSC, 0.2% bovine serum albumin (BSA), 10% dextran sulfate, 2 mM vanadyl adenosine complex, and 1 mg/ml each of yeast transfer RNA and salmon sperm DNA. After being washed three times for 30 min at 45°C with 50% formamide and 2× SSC, the probe was detected with anti-DIG antibody Fab conjugated with alkaline phosphatase (Roche) and visualized with HNPP/FastRed (Roche) according to the manufacture's protocol. After nuclei were stained with 4′, 6-diamidino-2-phenylindole (DAPI), sections were mounted with an aqueous mounting kit. The specificity of the RNA foci was confirmed both by detection of foci with different stringencies in experiments and by verification that they disappeared with RNase A treatment, but not with DNase. At least ten Purkinje cells were observed in each section.

Recombinant Glutathione-S-Transferase-Fused Splicing Factor Protein Synthesis and the Electrophoretic Mobility-Shift Assay

To further clarify the pathogenic implication of transcribed repeat insertion, we looked for proteins that could potentially bind to the transcribed repeats. Based on the fact that the SCA31 repeat sequence was related to satellite sequence in heterochromatin (see Results), and also based on consultation with ESEfinder 3.0, we found two serine/arginine-rich splicing factor proteins (SR proteins), SFRS1 and SFRS9, that were good candidates for binding to transcribed SCA31 insertions.

Recombinant GST-fused SR proteins were synthesized as follows. The cDNA of the full-length coding regions of SR proteins (SFRS1-1: NM_006924.4; SFRS1-2: NM_001078166.1; and SFRS9: NM_003769.2; all in NCBI) were amplified by PCR from a cDNA library of human cerebellum (Takara Bio) with custom primers (Table S4). SFRS1-1-R corresponds to SFRS1 isoform 1 (SFRS1-1) and SFRS1-2-R to SFRS isoform 2 (SFRS1-2). The PCR products were double digested with EcoRI and SalI and cloned in frame into the EcoRI-SalI site of the pGEX-6P1 vector (GE Healthcare Bioscience). The SR-protein constructs were first introduced into JM109, amplified, and then used for transforming the BL21 strain of *E. coli*.

The GST-fused SR proteins were harvested by a modified version of the previously described method.[24] In brief, 500 ml of transformed BL21 cell cultures was induced with 0.5–1.0 mM of IPTG for 3 hr, and the collected cells were suspended in 50 mM Tris-HCl (pH 8.0) and 150 mM NaCl. The *E. coli* were sonicated and treated with 0.02% DNase, 1 mg/ml lysozyme, and 1 mM PMSF. GST-fused proteins were purified from the soluble fraction with Glutathione Sepharose 4 Fast Flow (GE Healthcare Bioscience) and eluted with 50 mM Tris-HCl (pH 8.0) and 20 mM glutathione. After dialysis, the concentrations of the proteins were measured by BCA assay. GST-SFRS1-1 and GST-SFRS9 were successfully synthesized, whereas GST-SFRS1-2 was poorly collected in the soluble fraction. GST-SFRS1-1 was used as the representative of GST-SFRS1 in the subsequent study.

For electrophoretic mobility-shift assays (EMSAs), the synthetic RNA oligonucleotides, $(UGGAA)_8$, $(UAGAA)_8$, and $(UAGAAUA\ AAA)_4$, were labeled with digoxigenin (DIG). The RNA probes and the specific competitors, unlabeled $(UGGAA)_8$, $(UAGAA)_8$, and $(UAGAAUAAAA)_4$, were denatured at 94°C and immediately used for the following procedures. RNA probes (1.5 pmoles) were mixed with 2.4×10^{-7} g of either synthetic GST-fused protein or GST alone, different concentrations (0- to 100-fold the concentration of the probe) of one of the specific competitors, and 4 nM of poly [d(A-T)] in a 20 μl solution of 20 mM HEPES (pH 7.6), 1 mM EDTA, 10 mM $(NH_4)_2SO_4$, 1 mM DTT, 0.2% (w/v) Tween 20, and 30 mM KCl. The mixtures were incubated for 25 min at room temperature and then placed on ice. After dilution of the mixtures with 0.5× TBE buffer to give one-fifth of the original concentrations, the protein-bound probes were separated from the free forms by being run through 6% native polyacrylamide gels at 30 V in 0.5× TBE buffer. The separated RNA probes were transferred to positively charged nylon membranes by a semi-dry method and then detected with the DIG Luminescent Detection Kit (Roche) according to the manufacturer's instructions.

In Silico Location Search of Penta-Nucleotide Repeats

To reveal the origin of complex penta-nucleotide insertion, we searched locations in the human genome where repeat sequences $(TGGAA)_n$, $(TAGAA)_n$, and $(TAAAATAGAA)_n$ were abundantly present. For this purpose, repeat sequences were set unmasked, and then locations of $(TGGAA)_{40}$, $(TAGAA)_{40}$, and $(TAAAATA\ GAA)_3$ were searched for in the "reference only" human genome by BLAST. The best-matched 500 locations with E value < 0.0001 were selected and were shown in "genome view" according to the degree to which they matched. We then checked the matched sequences manually to confirm that pure stretches had been correctly selected. The resultant locations were shown in chromosome figures.

Mutation Screening in the SCA4 Family and 21 Disease Controls

To investigate the genetic relationship between SCA31 and SCA4, we screened five DNA samples from the American SCA4 family[7] by